

To appear in The Astrophysical Journal

Chandra and Spitzer Imaging of the Infrared Cluster in NGC 2071

Stephen L. Skinner and Kimberly R. Sokal

CASA, Univ. of Colorado, Boulder, CO, USA 80309-0389

S. Thomas Megeath

*Ritter Observatory, Dept. of Physics and Astronomy, University of Toledo, Toledo, OH
43606*

Manuel Güdel

Institute of Astronomy, ETH Zürich, Wolfgang-Pauli-Str. 27, 8093 Zürich, Switzerland

Marc Audard

Integral Science Data Centre, Ch. d'Ecogia 16, CH-1290 Versoix, Switzerland

*Geneva Observatory, University of Geneva, Ch. des Maillettes 51, 1290 Sauverny,
Switzerland*

Kevin M. Flaherty and Michael R. Meyer

*Steward Observatory, The University of Arizona, 933 N. Cherry Ave., Tucson, AZ, USA
85721-0065*

Augusto Damineli

*Instituto de Astronomia, Geofísica e Ciências Atmosféricas, Universidade de São Paulo,
Rua do Matão 1226, Cidade Universitária, 05508-900 São Paulo, SP, Brazil*

ABSTRACT

We present results of a sensitive *Chandra* X-ray observation and *Spitzer* mid-IR observations of the infrared cluster lying north of the NGC 2071 reflection nebula in the Orion B molecular cloud. We focus on the dense cluster core known as NGC 2071-IR which contains at least nine IR sources within a $40'' \times 40''$ region. This region shows clear signs of active star formation including

powerful molecular outflows, Herbig-Haro objects, and both OH and H₂O masers. We use *Spitzer* IRAC images to aid in X-ray source identification and to determine YSO classes using mid-IR colors. *Spitzer* IRAC colors show that the luminous source IRS 1 is a class I protostar. IRS 1 is believed to be driving a powerful bipolar molecular outflow and may be an embedded B-type star or its progenitor. Its X-ray spectrum reveals a fluorescent Fe emission line at 6.4 keV, arising in cold material near the protostar. The line is present even in the absence of large flares, raising questions about the nature of the ionizing mechanism responsible for producing the 6.4 keV fluorescent line. *Chandra* also detects X-ray sources at or near the positions of IRS 2, IRS 3, IRS 4, and IRS 6 and a variable X-ray source coincident with the radio source VLA 1, located just 2'' north of IRS 1. No IR data are yet available to determine a YSO classification for VLA 1, but its high X-ray absorption shows that it is even more deeply-embedded than IRS 1, suggesting that it could be an even younger, less-evolved protostar.

Subject headings: stars: individual (IRS 1) — open clusters and associations: individual (NGC 2071) — stars: formation — X-rays: stars

1. Introduction

The Lynds 1630 dark cloud (Lynds 1962) is located approximately 4' north of the optical reflection nebula NGC 2071 in the Orion B molecular cloud (Maddalena et al. 1986). L1630 was recognized as a site of recent star formation by Strom et al. (1975), who identified a young stellar population with an estimated age of a few million years containing early B and A-type stars, optically-revealed H α emission line stars (T Tauri stars), and several embedded infrared sources. An overview of star formation in the NGC 2071 region can be found in Gibb (2008).

The L1630 dark cloud was mapped at 2.2 μ m by Strom, Strom, & Vrba (1976) and 70 sources were detected down to a limiting magnitude $K \approx 10.7$ mag. About one-third of these lacked optical counterparts and they estimated an extinction $A_v \approx 20$ mag toward the cloud center. A more sensitive 2.2 μ m survey of L1630 was undertaken by Lada et al. (1991) who identified 912 sources down to $K \approx 13.0$ mag, about half of which were associated with L1630 itself.

Using known MK spectral types and optical photometry for a large sample of non-variable B star members, the distance to this region was estimated to be 390 pc by Anthony-Twarog (1982). But, the near and far edges of the Orion OB1 association span a range of

≈ 320 pc to 500 pc (Brown, de Geus, & de Zeeuw 1994; Wilson et al. 2005). Using *Spitzer* IRAC and MIPS data along with low-resolution optical spectra, Flaherty & Muzerolle (2008) determined a cluster age of 2 ± 1.5 Myr and concluded that 79% of the late-type cluster members in their sample have infrared excesses. They found evidence for active accretion in all of the IR-excess objects.

The extended NGC 2071 cluster identified by Lada et al. (1991) covers an area of ≈ 80 arcmin² and contains a dense subgroup known as NGC 2071-IR (Figs. 1 and 2) which harbors at least nine IR sources in a $40'' \times 40''$ core region (Walther, Geballe, & Robson 1991; Walther et al. 1993, hereafter W93; Tamura et al. 2007, hereafter T07). The position of NGC 2071-IR within NGC 2071 is shown in Figure 2 of W93 and a wide-field perspective showing the location of this region within the Orion complex can be found in Fig. 3 of Maddalena et al. (1986). Within NGC 2071-IR, the bright infrared source IRS 1 is of particular interest. The nature of this object is unclear but previous studies have concluded it may be a young embedded B-type star (W93; Snell & Bally 1986). The NGC 2071-IR subgroup shows clear signs of active star-formation including powerful bipolar molecular outflows (Bally 1982; Snell et al. 1984; Aspin, Sandell, & Walther 1992; Eislöffel 2000), Herbig-Haro objects (Zhao et al. 1999), and water masers near IRS 1 and IRS 3 (Torrelles et al. 1998) and IRS 2 (Sandell et al. 1985). An OH maser has been detected within $\approx 20''$ of IRS 1 (Johansson et al. 1974; Pankonin et al. 1977; Sandell et al. 1985) but the maser position is not well-enough known to determine if it is coincident with IRS 1. *VLA* maps in NH₃ lines reveal what appears to be a large ring structure or edge-on disk surrounding NGC 2071-IR (Zhou, Evans, & Mundy 1990).

More than one outflow may be present in NGC 2071-IR. Using H₂ 1-0 S(1) images, Eislöffel (2000) identified at least three outflows. These include an east-west outflow that may be driven by IRS 1 (see also Aspin, Sandell, & Walther 1992), and further support for such an outflow comes from high-velocity knots revealed in recent 3.6 cm *VLA* images (Carrasco-González et al. 2007). Eislöffel (2000) also concluded that there is an outflow oriented in the northeast-southwest direction that may be driven by IRS 3, and a third outflow close to IRS 7. Additional evidence that IRS 3 is driving an outflow comes from extended jet-like structure visible in high-resolution *VLA* radio continuum images (Torrelles et al. 1998). Aspin et al. (1992) argued that IRS 2 may also be driving a compact bipolar outflow. More recently, Stojimirović et al. (2008) have reported evidence for at least three outflows in the NGC 2071 region based on moderate resolution (HPBW $\approx 45''$) ¹²CO and ¹³CO $J = 1 \rightarrow 0$ molecular line maps. However, the association of individual outflows with specific driving sources remains somewhat uncertain due to the complex morphology of the region.

A previous X-ray observation of the NGC 2071 region with *XMM-Newton* detected a prominent X-ray source at a position within $1''$ of IRS 1 (Skinner et al. 2007, hereafter S07). The X-ray source was identified with IRS 1, but was subject to limitations on source identification in the crowded cluster core imposed by *XMM*'s $\approx 4''$ angular resolution. We present here the results of a higher angular resolution *Chandra* X-ray observation of NGC 2071-IR. Our main objectives were to confirm the previous X-ray detection of IRS 1 with improved positional accuracy and identify possible mechanisms for its X-ray emission. Although the X-ray emission of optically-revealed OB stars has been extensively studied and is thought arise in shocked winds, much less is known about X-ray production in very young embedded high-to-intermediate mass stars such as IRS 1. We confirm that IRS 1 is indeed an X-ray source and discuss its X-ray properties along with several other X-ray detections in the NGC 2071-IR subgroup (IRS 2, IRS 3, IRS 4, and IRS 6). *Chandra*'s sharp angular resolution also reveals a new X-ray source associated with the radio continuum source VLA 1 lying $2.''2$ north of IRS 1. The VLA 1 X-ray source is seen through very high absorption equivalent to $A_V \sim 40$ mag, suggesting that it is a young heavily-embedded protostar. We also use *Spitzer* observations and previous near-IR observations to identify IR counterparts to the X-ray sources and determine their IR spectral energy distributions. We also use IR color-color diagrams to assign young stellar object (YSO) classes.

2. Observations

2.1. Chandra Observations

The *Chandra* observation (ObsID 7417) began on 2007 November 6 at 19:40:19 TT and ended on November 7 at 15:18:03 TT. Pointing was centered near NGC 2071 IRS 1 at nominal pointing coordinates (J2000) RA = $05^h 47^m 04.94s$, Dec. = $+00^\circ 22' 11.8''$. The exposure live time was 67,180 s. Exposures were obtained using the ACIS-I (Advanced CCD Imaging Spectrometer) imaging array in faint timed-event mode with 3.2 s frame times. ACIS-I has a combined field of view (FOV) of $\approx 16.9' \times 16.9'$ consisting of four front-illuminated 1024×1024 pixel CCDs with a pixel size of $0.492''$. Approximately 90% of the encircled energy at 1.49 keV lies within $2''$ of the center pixel of an on-axis point source. Our discussion here focuses on ACIS-I, but the S2 and S3 CCDs in the ACIS-S array were also enabled. More information on *Chandra* and its instrumentation can be found in the *Chandra* Proposer's Observatory Guide (POG)¹.

¹See <http://asc.harvard.edu/proposer/POG>

The Level 1 events file provided by the *Chandra* X-ray Center (CXC) was processed using CIAO version 3.4² using standard science threads. The CIAO processing applied calibration updates (CALDB vers. 2.26), selected good event patterns, and determined source centroid positions.

Additionally, we used the CIAO *wavdetect* tool to identify X-ray sources on the ACIS-I array. We ran *wavdetect* on full-resolution images using events in the 0.3-7 keV range to reduce the background. The *wavdetect* threshold was set at *sighthresh* = 1.5×10^{-5} and scale sizes of 1, 2, 4, 8, and 16 were used. We identified 207 X-ray sources on ACIS-I down to a threshold of 5 counts, including the sources of primary interest in this work located in the NGC 2071-IR core region listed in Table 1.

The unabsorbed X-ray luminosity upper limit for non-detections is $\log L_X$ (0.3 - 7 keV) ≤ 28.7 ergs s⁻¹. This upper limit from the Portable Interactive Multi-Mission Simulator (PIMMS)³ assumes a 5 count on-axis detection threshold and an absorbed isothermal optically thin plasma spectrum similar to that observed for IRS 1 ($N_H = 2 \times 10^{22}$ cm⁻², kT = 2 keV). At this upper limit, the observation was sensitive enough to detect low-mass T Tauri stars in Orion down to $\approx 0.1 - 0.2 M_\odot$, based on the known correlation between L_X and stellar mass in T Tauri stars (Preibisch et al. 2005). The above upper limit should be considered as a representative value since the detection limit depends on many factors including the spectral properties of the source and extent to which the source is displaced off-axis.

At the sensitivity of our observation, we expect ≈ 1 extragalactic background source in a region spanning ≈ 1.6 arcmin², or < 1 extragalactic source in the $\approx 40'' \times 40''$ NGC 2071-IR region analyzed here. This estimate is based on hard-band (2 - 8 keV) number counts from the *Chandra* deep field (CDF) and other X-ray surveys (e.g. Brandt et al. 2001; Moretti et al. 2003) and an assumed power-law spectrum with a photon power-law index $\Gamma = 1.4$ for extragalactic sources. The above estimate should be considered as approximate because the accuracy of the $\log N - \log S$ distribution for extragalactic sources based on deep-field observations when applied to lower galactic latitude star-forming regions is not well-known. Getman et al. (2005) concluded that CDF number counts overestimated the number of extragalactic sources in the deep *Chandra* COUP observation of the Orion Nebula Cluster by a factor of $\sim 3 - 4$.

²Further information on *Chandra* Interactive Analysis of Observations (CIAO) software can be found at <http://asc.harvard.edu/ciao>.

³Information on PIMMS can be found at <http://asc.harvard.edu/ciao/ahelp/pimms.html>.

CIAO *psextract* was used to extract source and background spectra for brighter sources, along with source-specific response matrix files (RMFs) and auxiliary response files (ARFs) used in spectral fitting. Light curves of brighter sources were also extracted using CIAO tools. We used the 3σ source ellipses from *wavdetect* to define the extraction regions and background was extracted from adjacent source-free regions. Background is negligible, contributing only 0.21 counts per pixel (0.3 - 7 keV) for the total exposure time, or less than one count in the regions used to extract source spectra and light curves. Spectral fitting and timing analysis were undertaken with the HEASOFT *Xanadu*⁴ software package including XSPEC vers. 12.4.0. We also applied the Kolmogorov-Smirnov (KS) test (Press et al. 1992) to unbinned photon arrival times to check for X-ray variability.

Since conventional spectral fitting is only practical for brighter sources, we used the quantile analysis approach of Hong et al. (2004) to quantify source hardness. This technique has the advantage that it can be applied to sources that are too faint for spectral fitting. The quantile method uses sorted photon event energy lists to compute the median energy $E_{50\%}$ and the quartile energies $E_{25\%}$ and $E_{75\%}$. The quartile energies are defined such that one-fourth of the counts have energies below $E_{25\%}$, and three-fourths below $E_{75\%}$. The quantile fractions Q_x are computed from quartile energies using $Q_x = (E_{x\%} - E_{lo}) / (E_{up} - E_{lo})$, where E_{lo} and E_{up} are the lower and upper energy bounds of the extracted events (0.3 and 7.0 keV in this work). Quantile values (or functions thereof) are then overplotted on a grid of neutral hydrogen absorption column density (N_H) and plasma energy (kT) values generated from spectral simulations based on a one-temperature (1T) APEC optically thin thermal plasma model. This provides a graphical representation of the source hardness superimposed on a (N_H , kT) grid that is akin to an X-ray color-color diagram.

2.2. Spitzer Observations

We use infrared observations of the NGC 2071-IR region obtained by the *Spitzer Space Telescope* to aid in X-ray source identification and to determine YSO classes using mid-IR colors. *Spitzer*'s Infrared Array Camera (IRAC) mapped the NGC 2071-IR region as part of *Spitzer* Orion Survey (GTO program ID 043; Megeath et al. 2005a; Allen et al. 2007; Flaherty & Muzerolle 2008; Megeath et al. 2009, in prep.) Further information on IRAC can be found in Fazio et al. (2004). The IRAC data were obtained in four channels (3.6, 4.5, 5.8, and 8.0 μm) using the high-dynamic range (HDR) mode, acquiring a short 0.6 s exposure plus a longer 12 s exposure at each pointing position. Four dithers were obtained

⁴<http://heasarc.gsfc.nasa.gov/docs/xanadu/xanadu.html>.

at each position.

The reduction and analysis of the complete data set will be discussed in detail by Megeath et al. (2009, in prep.). In brief, individual basic calibrated data (BCD) frames were mosaicked with custom software to create separate mosaic images for the four IRAC channels. Point sources were identified using PhotVis v. 1.10 (Gutermuth et al. 2004; Gutermuth et al. 2008). Using the source positions determined from the mosaics, photometry was measured for each point source on the individual BCD images using the IDL module *aper.pro* (Landsman 1993). Magnitudes were measured in a circular aperture of radius $r = 2$ pixels centered on the source, using a background annulus of $r = 2 - 6$ pixels. A gain correction depending on pixel position was applied to each magnitude. The final magnitudes are the median magnitude returned from the four dithers. Magnitudes of those sources in the NGC 2071-IR region discussed here are given in Table 2, along with magnitude zero points and aperture correction factors.

Spitzer MIPS data at longer wavelengths 24 - 160 μm are also available (Flaherty & Muzerolle 2008; Megeath et al. 2009, in prep). Because the NGC 2071-IR region is confused and heavily saturated, we only provide here the MIPS 24 μm photometry for IRS 7. MIPS data were reduced using the procedure given in Megeath et al. (2009).

3. Results

We focus here on the heavily-reddened NGC 2071-IR subgroup shown in the 2MASS 2.16 μm (K_s) image in Figure 1 and the *Spitzer* IRAC 3.6 μm (ch1) image in Figure 2. This region of high source density includes the infrared sources IRS 1 - 8 and IRS 8a (W93; T07), as well as the radio source VLA 1 located near IRS 1. We summarize the IR and X-ray properties of each source on an individual basis below.

Figure 3 shows near-IR colors of IRS 1-8, all of which show some excess reddening. Figure 4 is an IRAC color-color diagram that provides one means of distinguishing between class I YSOs (protostars) and class II YSOs (classical T Tauri stars, or accreting star+disk systems). Figure 5 plots the infrared spectral energy distributions (SEDs) of those sources in NGC 2071-IR for which reliable near-IR and *Spitzer* mid-IR data are available (IRS 1, IRS 2, IRS 4, IRS 6, IRS 7). Figure 6 shows the broad-band *Chandra* ACIS-I image for the central region of NGC 2071-IR near IRS 1, and Figure 7 is a hard-band *Chandra* image zoomed in on IRS 1 and VLA 1. Figure 8 is a quantile diagram allowing the X-ray properties of *Chandra* detections to be compared.

Table 1 summarizes the properties of the X-ray sources detected by *Chandra*, and *Spitzer*

IRAC photometry is given in Table 2. *Chandra* detected X-ray sources at or near the positions of IRS 1,2,4,6 and VLA 1. The infrared sources IRS 5,7, 8, and 8a (offset $\approx 2''$ northeast of IRS 8) were undetected by *Chandra*. Table 3 summarizes X-ray spectral analysis results for the brighter detections.

3.1. IRS 1

IRS 1 was identified as a bright $10\ \mu\text{m}$ source by Persson et al. (1981). It is also clearly visible in the 2MASS K_s image (Fig. 1) and in *Spitzer* IRAC images (Fig. 2). A very bright source at or near the position of IRS 1 saturates the MIPS $24\ \mu\text{m}$ images. IRS 1 is likely the dominant contributor to the mid/far-IR luminosity toward the NGC 2071-IR region, which was determined to be $L_{\text{tot}} = 520\ L_{\odot}$ ($d = 390\ \text{pc}$) by Butner et al. (1990). This luminosity suggests that IRS 1 may be an embedded early-type star, as discussed further in Section 5.1. But, its true nature is still somewhat of a mystery.

IRS 1 is clearly detected in all four IRAC channels and its SED rises sharply toward longer wavelengths over the $3.6\ \mu\text{m} - 8.0\ \mu\text{m}$ IRAC range (Fig. 5). It is the brightest IR source in the NGC 2071-IR core region at $8.0\ \mu\text{m}$ (Table 3). *Spitzer*'s angular resolution of $\text{FWHM} \approx 1.7''$ ($3.6\ \mu\text{m}$) is unable to fully resolve VLA 1 located $2.2''$ north of IRS 1. But, the IRAC images do show what appears to be faint emission extending northward of IRS 1, providing a clue that VLA 1 may be weakly contributing to the mid-IR flux measured inside the $r = 2.''4$ aperture centered on IRS 1. Higher angular resolution mid-IR observations will be needed to confirm that VLA 1 is indeed a mid-IR source.

The IRAC colors of IRS 1 are characteristic of a class I protostar (Fig. 4). Adopting the YSO classification scheme of Gutermuth et al. (2008), class I sources are defined by $[4.5] - [5.8] > 1$, where brackets denote magnitudes at the enclosed wavelength (μm). IRS 1 has $[4.5] - [5.8] = 1.67$ (Table 3), so the class I criterion is satisfied. A similar conclusion is reached using the YSO classification schemes of Allen et al. (2004), Hartmann et al. (2005), and Megeath et al. (2005b).

Chandra detects an X-ray source that is offset by only $0.42''$ from the near-IR position of IRS 1 ($= 2\text{MASS J054704.77+002142.8}$). This offset is within *Chandra* positional uncertainties and we thus associate X-ray source CXO J054704.75+002142.9 with the infrared source IRS 1. The IRAC $3.6\ \mu\text{m}$ detection of IRS 1 has a centroid position J054704.76+002143.0, which is offset by only $0.18''$ from the *Chandra* X-ray position. This *Chandra* detection confirms that IRS 1 is an X-ray source, as suspected on the basis of the previous lower spatial resolution *XMM-Newton* observation (S07).

The X-ray light curve of IRS 1 (Fig. 9) shows low-amplitude fluctuations about the mean at the $\pm 2\sigma$ level but no large flares. The KS test gives a probability of constant count rate $P_{\text{const}} = 0.11$. Thus, low-level variability may be present but is not proven at high confidence levels.

IRS 1 is clearly detected in the hard-band ACIS-I image (Fig. 7) but its emission is not as hard as that of VLA 1 or IRS 3 as gauged by median photon energy (Table 1). The X-ray spectrum of IRS 1 (Fig. 10) is absorbed below 1 keV but the absorption is not as high as that of VLA 1. The ACIS-I spectrum of IRS 1 shows an emission line from the Si XIII He-like triplet complex (1.839 - 1.865 keV), implying thermal emission. Maximum power for the Si XIII triplet is emitted at $\log T_{\text{max}} = 7.0$ (K) so hot plasma is clearly detected. The spectrum also reveals a faint (7 counts) fluorescent emission line at ≈ 6.4 keV from neutral or low ionization stages of Fe (Fig. 11), as anticipated from *XMM-Newton* spectra. This line forms in “cold” material in the vicinity of the star that is irradiated by the hard X-ray source and is discussed further in Section 5.3.

We attempted to fit the ACIS-I spectrum of IRS 1 with various emission models. All models included a fixed-width Gaussian line at 6.4 keV to reproduce the faint fluorescent Fe line. A simple one-temperature (1T) APEC solar abundance optically thin plasma model underestimates the flux in the 1.7 - 1.9 keV range and is unacceptable in terms of χ^2 statistics. This range includes the Si XIII He-like triplet lines at 1.839, 1.854, and 1.865 keV, which cannot be individually distinguished at the spectral resolution of ACIS-I. An acceptable 1T fit can be obtained by allowing Si to be overabundant by a factor of ~ 3 with respect to its solar value. The apparent Si overabundance could either be a real physical effect due to factors such as grain destruction (e.g via grain-grain collisions in shocks) or an unphysical consequence of fitting the spectrum with an overly simplistic 1T model.

An acceptable solar abundance fit can be obtained with a two-temperature (2T) APEC model that includes both a cool and hot plasma component (Table 3). Some further improvement in the 2T fit can be obtained by allowing Si to be overabundant, but this is not required since the solar abundance fit is already statistically acceptable ($\chi^2_{\text{red}} = 1.01$). Because of the heavy absorption below 1 keV, the temperature and emission measure of any cool component are quite uncertain. The 2T APEC model summarized in Table 3 uses a fixed temperature $kT_1 = 0.55$ keV for the cool component. This temperature results in a minimum value of the C-statistic (Cash 1979) when fitting unbinned spectra. However, there is very little change in the C-statistic for values in the range $kT_1 = 0.25 - 0.70$ keV. The 2T model yields a best-fit temperature for the hot plasma component $kT_2 = 3.3$ keV, but the true temperature could be higher since the 90% confidence upper limit is not tightly constrained by the data. Using the conversion $N_{\text{H}} = 2.22 \times 10^{21} \text{ A}_V \text{ cm}^{-2}$ (Gorenstein

1975), the solar abundance 2T APEC model gives $A_V = 16$ [12 - 20] mags, where square brackets enclose the 90% confidence range. The slightly different conversion $N_H = 1.6 \times 10^{21} A_V \text{ cm}^{-2}$ (Vuong et al. 2003) yields $A_V = 22$ [16 - 28] mags. The standard conversions used above are reliable for low-extinction sources, but some studies have questioned their accuracy for deeply-embedded YSOs (Winston et al. 2007).

The above APEC model assumes that the X-ray emission arises in an optically thin thermal plasma and is typically used to model coronal emission in magnetically active late-type stars. However, other emission processes might be operating in IRS 1. In particular, X-rays could be produced in shocks associated with its powerful outflow. Thus, we tried to fit the IRS 1 spectrum with an isothermal plane-parallel shock model (VPSHOCK). The fit statistic for VPSHOCK ($\chi^2_{red} = 1.16$) is not quite as good as the 2T APEC model and the fit converges to shock temperatures $kT \approx 2 - 3$ keV (Table 3). Such shock temperatures are realistic but do require high-velocity flows, as discussed further in Section 5.2.1.

In summary, a 1T APEC thermal plasma model is able to reproduce the *Chandra* spectrum of IRS 1 provided that Si is allowed to be overabundant. An acceptable solar-abundance fit can be obtained with a 2T APEC model, but it does not tightly constrain the temperature or emission measure of the heavily-absorbed cool component. This model requires hot plasma at $kT_2 \approx 3$ keV and an absorption column density equivalent to $A_V \approx 16 - 22$ mags.

3.2. VLA 1

VLA 1 is a compact 3.6 cm radio continuum source revealed in high-resolution VLA A-configuration images obtained by Carrasco-González et al. (2007). It was also marginally detected in previous 5 GHz VLA images shown in Snell & Bally (1986). The 3.6 cm radio source is located $2.2''$ north of IRS 1, which equates to a projected separation of ≈ 860 AU at $d = 390$ pc.

The *Chandra* X-ray position is in very good agreement with the radio position of VLA 1 (Table 1). Due to its close proximity to IRS 1, VLA 1 was not spatially resolved from IRS 1 by *XMM-Newton*. We are not aware of any published high-resolution infrared images which show that VLA 1 is an infrared source. But, *Spitzer* images (Fig. 2) reveal faint northward extension from IRS 1 that may be due to VLA 1.

The KS test shows that the X-ray emission of VLA 1 is likely variable with $P_{const} = 0.02$, though the lightcurve shows no large amplitude flares (Fig. 9). The ACIS-I spectrum is heavily absorbed with little or no X-ray emission detected below 2 keV. The spectrum can

be acceptably fitted with a 1T APEC model at $kT = 2.2$ keV (Table 2). No significant Fe line emission is detected in the 6.4 - 6.7 keV range. The inferred absorption column density $\log N_H = 22.94$ gives an equivalent extinction $A_V = 39$ [22 - 69] mag using the Gorenstein (1975) conversion. Based on X-ray spectral fits, VLA 1 is more heavily absorbed than IRS 1 and Figure 8 indicates that it is the most heavily absorbed X-ray source in NGC 2071-IR. VLA 1 could thus be in an earlier evolutionary stage than IRS 1. Because of the high absorption the intrinsic (unabsorbed) X-ray luminosity of VLA 1 is quite uncertain. But, the value inferred from the 1T APEC model (Table 2) is consistent with that of a \sim solar-mass pre-main sequence star or protostar, based on the known correlation between L_X and stellar mass in low-mass YSOs (Preibisch et al. 2005; Telleschi et al. 2007a).

3.3. IRS 2

Previous studies have concluded that IRS 2 is likely a young stellar object (W93; T07) and Aspin et al. (1992) argued that it is driving a bipolar outflow. IRAC images show some indication that the source is extended. IRAC colors (Fig. 4) indicate that IRS 2 is either a class I protostar or a heavily-reddened class II object. However, some caution is warranted in interpreting IRAC colors. High-resolution 3.6 cm radio continuum observations reveal two closely-spaced components A and B separated by $\approx 1.''4$ with the brighter component A at radio position VLA J054705.367+002150.5 (Carrasco-González et al. 2009, private comm.). *Spitzer* cannot resolve such a close pair and it is thus possible that the IRAC colors are the superposition of two sources.

Chandra detects a very faint X-ray source (4 net counts) at an offset of only $0.27''$ from the brighter radio component A (Table 1). Because of the good positional coincidence with the radio source, this weak X-ray detection is likely real but is of marginal significance. There are too few counts to do any substantive X-ray analysis but the high median photon energy $E_{50} = 5.2$ keV suggests that this source is exceptionally hard or very heavily absorbed.

3.4. IRS 3

The infrared source IRS 3 is about one magnitude fainter at K-band and at $3.6 \mu\text{m}$ and $4.5 \mu\text{m}$ than IRS 1. Its K band emission is highly polarized (W 93; T07). A 1.3 cm radio continuum source lies near IRS 3 (Torrelles et al. 1998), but the near-IR peak is offset slightly to the northeast relative to the *VLA* radio position (T07). As Table 1 shows, the weak X-ray source detected by *Chandra* is in excellent positional agreement with the 1.3

cm radio source detected by Torrelles et al. (1998). The nearest 2MASS source lies $2.3''$ from the X-ray peak. This offset is significant and supports the conclusion of T07 that the near-IR emission is nebulosity. The object detected with *Chandra* and the *VLA* is likely the star that illuminates the near-IR nebula. *Spitzer* IRAC images show an infrared source near IRS 3 (Fig. 2). The IRAC position as measured in the $4.5\ \mu\text{m}$ (ch2) image is offset by only $0.42''$ from *Chandra*. Thus, it appears that the self-luminous source is also detected by *Spitzer*. We do not have complete IRAC photometry for IRS 3 because it lies in the bright wings of IRS 1.

A KS test shows no significant X-ray variability. The distribution of event photon energies (Fig. 12) shows clearly that this is a hard absorbed source, and the energy quantile plot (Fig. 8) substantiates this. There were too few counts to analyze a binned spectrum but we did attempt to fit the unbinned spectrum with a 1T APEC thermal plasma model using C-statistics (Cash 1979). The absorption was held fixed at $\log N_{\text{H}} = 22.79\ \text{cm}^{-2}$, based on the estimated extinction $A_V = 28\ \text{mag}$ (W93). The fit converges to a high but uncertain temperature $kT \gtrsim 10\ \text{keV}$, as also indicated by the quartile plot (Fig. 8).

Visual inspection of the unbinned spectrum shows a weak buildup of counts near 6.4 keV, hinting that a weak fluorescent Fe line may be present. The IRS 3 event list reveals five events within the 6 - 7 keV range with event energies 6.11, 6.20, 6.42, 6.53, and 6.69 keV. The 6.42 and 6.53 keV events could be due to fluorescent Fe. We added a Gaussian line component to the 1T APEC model at a line energy of 6.4 keV, fixing the line width at $\text{FWHM} = 120\ \text{eV}$, corresponding to the ACIS-I instrumental width at this energy (*Chandra* POG, Fig. 6.8). With the Gaussian line included, the C-statistic $C = 133.1$ is slightly less than without the line ($C = 138.2$), and the fit gives $\log N_{\text{H}} = 22.79\ \text{cm}^{-2}$, $kT = 10\ \text{keV}$, and an unabsorbed flux $F_{X,\text{unabsorbed}}(0.5 - 7.5\ \text{keV}) = 1.6 \times 10^{-14}\ \text{ergs cm}^{-2}\ \text{s}^{-1}$. This equates to $\log L_X = 29.5\ \text{ergs s}^{-1}$ ($d = 390\ \text{pc}$), which is typical of low-mass YSOs in Orion (Preibisch et al. 2005). Thus, the event list and spectral fits provide some marginal evidence for fluorescent Fe, but a deeper exposure would be needed to make a compelling case for a 6.4 keV line detection.

The high-resolution *VLA* 1.3 cm radio continuum images of IRS 3 obtained by Torrelles et al. (1998) show elongation in the \approx N-S direction, and elongated morphology is also visible in the more recent 3.6 cm *VLA* images of Carrasco-González et al. (2007). The extension was interpreted as a thermal radio jet, adding support to the belief that IRS 3 is driving an outflow (Sec. 1). The orientation of H_2O maser spots approximately perpendicular to the jet axis and maser velocity data led Torrelles et al. (1998) to conclude that the masers trace a compact rotating molecular disk surrounding a low-mass ($\sim 1\ M_{\odot}$) YSO. Such a disk viewed in a nearly edge-on geometry would act as a strong absorber of soft X-ray photons and would

provide a natural explanation for the high N_{H} (Fig. 8) and lack of detected low-energy X-ray photons below ~ 2 keV in IRS 3 (Fig. 12).

3.5. IRS 4

Tamura et al. (2007) concluded that IRS 4 is an IR cluster member because it is surrounded by a compact reflection nebula and is associated with faint H_2 emission. The faint X-ray source detected by *Chandra* is in good positional agreement with 2MASS and shows no significant variability. It has the lowest median and mean photon energy of the six X-ray sources detected in the cluster core. There are insufficient counts available for spectral analysis. About half of the detected photons have energies below 2 keV. Quantile analysis shows that this source has lower absorption than the other X-ray detections in NGC 2071-IR (Fig. 8). Near-IR colors (Fig. 3) are consistent with a star having intrinsic cTTS color but viewed through substantial reddening ($A_{\text{V}} \approx 13$ mag). IRAC colors (Fig. 4) are consistent with a reddened class II YSO but the SED (Fig. 5) is nearly flat in the IRAC bands and is more suggestive of a flat-spectrum source.

3.6. IRS 5

The near-IR morphology of this infrared source changes with time and W93 concluded that the near-IR emission could be from a jet, a moving clump of shocked gas, or nebulosity. IRS 5 is located between the two nearby bright mid-IR sources IRS 1 and IRS 2. We were not able to identify a definite point source at the IRS 5 position in the IRAC images, and thus cannot provide any reliable IRAC photometry. No significant X-ray emission was detected so we find no evidence of a young star and our results are thus consistent with the non-stellar classification proposed by W93.

3.7. IRS 6

Near-IR observations have shown that IRS 6 is a binary with a $2''$ separation (T07). We detect a variable X-ray source that is offset to the northwest of the 2MASS position by $1.68''$ at position angle $\text{PA} = 315^\circ$ (Table 1). This offset is significant and implies that the 2MASS near-IR source is not the same source detected in X-rays. *Spitzer* images show an IRAC source at an offset of $1.19''$ from the *Chandra* position. IRS 6 has similar near-IR and mid-IR colors to IRS 4, and both the near-IR and mid-IR colors of IRS 6 are consistent with

a reddened class II object (cTTS).

The spectral fit of IRS 6 with a 1T APEC thermal model (Table 2) suggests a rather hot source with plasma temperature $kT = 3.85$ keV and moderate absorption $N_H \sim 10^{22}$ cm $^{-2}$. Similar values are inferred from the quantile plot (Fig. 8), but both kT and N_H have rather large uncertainties due to the low number of X-ray counts. The absorption from the IRS 6 spectral fit (Table 2) gives an equivalent extinction $A_V = 5.6$ [1.7 - 10.4, 90% conf.] mag (Gorenstein 1975 conversion), which is less than IRS 1 and VLA 1.

On the basis of its relatively high kT and variability, we conclude that the X-ray source lying 1."68 from the 2MASS position is a magnetically-active star. Because this system is a close near-IR pair, higher spatial resolution observations are needed to confirm the IR colors and more accurately determine the relative positions of the two near-IR sources and the X-ray source.

3.8. IRS 7

Tamura et al. (2007) argued on the basis of polarization angle that circumstellar material is present around IRS 7. IRAC colors support this conclusion, indicating either a class I protostar or a heavily-reddened class II source (Fig. 4). The object is visible in MIPS 24 μ m images and the SED continues to rise out to 24 μ m (Fig. 5). Its [4.5] – [24] color is consistent with a protostar (Megeath et al. 2009). We detect no X-ray emission at or near IRS 7, so it is either intrinsically X-ray faint or its emission is reduced to undetectable levels by high absorption (e.g. a nearly edge-on disk or dense surrounding envelope).

3.9. IRS 8 and 8a

IRS 8 and 8a are two faint closely-spaced IR sources separated by 1.6" in RA and 0."7 in Dec, with IRS 8a lying northeast of IRS 8 (W93; T07). Both objects are >1.5 mag fainter at K than the other core sources (T07). The closest 2MASS positional match to IRS 8 has $K_s = 13.54$ (2MASS J054704.45+002138.8) and there are no other 2MASS sources within 5". IRS 8 is associated with a near-IR nebula and was classified as a self-luminous object, probably an embedded star, by W93. IRS 8a is thought to be a shocked molecular hydrogen peak (W93).

The IRAC images reveal what appears to be extended structure or nebulosity in the NE-SW direction near IRS 8. A faint emission peak is visible close to the IRS 8 position at 3.6 μ m (Table 2) and the peak shifts slightly to the northeast in the 4.5 μ m image,

which is sensitive to shock emission. The close pair IRS 8/8a is not clearly resolved at IRAC’s resolution, but the slight shift of the $4.5\ \mu\text{m}$ emission peak toward IRS 8a may be an indication that it is a stronger shock-excited source. Because of the nebulous morphology in IRAC images, we were not able to obtain any reliable IRAC photometry. There is no X-ray emission at or near the 2MASS position of IRS 8 or at IRS 8a, and consequently no X-ray evidence of an embedded star.

4. Comparison with XMM-Newton Results

The *XMM-Newton* EPIC CCD spectrum of IRS 1 analyzed by S07 was extracted using a nominal circular region of radius $R_e = 15''$ (68% encircled energy) centered on IRS 1. As the higher angular resolution *Chandra* image in Figure 6 shows, four X-ray sources were included in the *XMM-Newton* spectral extraction region, namely IRS 1,2,3 and VLA 1. Of these four, IRS 1 (144 counts) and VLA 1 (90 counts) are the brightest NGC 2071-IR core objects in the *Chandra* image. IRS 2 (4 counts) is very faint in ACIS-I and it is unlikely that it significantly affected the *XMM-Newton* spectrum. IRS 3 (18 counts) is also a faint hard *Chandra* source. Its absorbed flux F_X (0.5 - 7.5 keV) $= 8 \times 10^{-15}\ \text{ergs cm}^{-2}\ \text{s}^{-1}$ would have contributed $\approx 5\%$ to the observed flux measured in the *XMM-Newton* pn spectrum.

Based on the above, it is clear that the *XMM-Newton* spectrum was dominated by emission from the close pair IRS 1 and VLA 1. The *Chandra* data show that VLA 1 has much higher X-ray absorption than IRS 1, which explains why fits of the *XMM-Newton* pn spectrum mysteriously required two spectral components with different N_H values (S07).

The fluorescent Fe line at 6.4 keV was strongly detected in the *XMM* pn spectrum with an EPIC pn line flux F_X (6.2 - 6.6 keV) $= 3.8 (\pm 0.2) \times 10^{-14}\ \text{ergs cm}^{-2}\ \text{s}^{-1}$ and an equivalent width (EW) measured relative to the underlying continuum $\text{EW} = 2.4\ \text{keV}$ (S07). The line flux measured in the *Chandra* ACIS-I spectrum (Table 3) is a factor of ~ 5 below the *XMM* value, but the *Chandra* $\text{EW} \geq 2.4\ \text{keV}$ is consistent with the *XMM* value. The fluorescent Fe line is discussed further in Section 5.3.

5. Discussion

5.1. Is IRS 1 a Young Embedded B-type Star?

The heavily-reddened IRAC colors of IRS 1 and its rising SED in the IRAC bands, along with its bright (saturated) detection in MIPS $24\ \mu\text{m}$ images, strongly suggest that it

is a class I protostar. Based on its association with a radio continuum source and luminosity considerations, W93 concluded that IRS 1 is most likely a B0-B5 star. Under the assumption that the 6 cm radio continuum emission of IRS 1 arises in a photoionized compact H II region at a distance of 500 pc, Snell & Bally (1986) found that a single B2 star would be needed to produce sufficient Lyman continuum ionizing flux to account for the radio emission. Adjusting their distance downward to 390 pc (Anthony-Twarog 1982) would require a \sim B3 star. However, we note that the volume emission measure of the radio continuum source computed from their 6 cm radio flux density $S_{6cm} = 7.9$ mJy is two orders of magnitude below that typically found for optically thin compact HII regions (eq. [3] of Skinner, Brown, & Stewart 1993). Thus, the radio continuum emission from IRS 1 could very well involve processes other than free-free emission from a compact HII region.

The more recent high-resolution 3.6 cm *VLA* A-configuration images of IRS 1 obtained by Carrasco-González et al. (2007) reveal a complex source morphology for IRS 1. A compact core is present along with fainter emission extending in the E-W direction. More interestingly, compact knots are seen expanding away from IRS 1 in an approximate E-W direction with high velocities of up to ~ 600 km s $^{-1}$, as determined from radio proper motions. These results, along with the positive radio spectral index, suggest that the radio emission includes a contribution from an extended ionized wind or jet. A possible analog is NGC 7538-IRS1, whose free-free emission is dominated by a highly collimated ionized jet (Sandell et al. 2009).

Using far-IR data obtained with the *Kuiper Airborne Observatory* (KAO), Butner et al. (1990) determined the total luminosity toward the NGC 2071-IR region to be $L_{tot} = 520 L_{\odot}$ ($d = 390$ pc). This is about 15% greater than the value determined by Harvey et al. (1979) when normalized to a common distance of 390 pc. Because of the rather large $\approx 30''$ KAO beam size, this total will include any contributions from other sources near IRS 1 and should thus be considered an upper limit for IRS 1 itself. If due to a single star, a value $L_{tot} = 520 L_{\odot}$ would correspond to a ZAMS star of mass $\sim 5 M_{\odot}$ (Siess, Dufour, & Forestini 2000) and ZAMS spectral type \sim B4 (Thompson 1984). But, if the L_{tot} value is interpreted as an upper limit for IRS 1, a lower mass and later spectral type are possible. The above estimates are based on an assumed distance $d = 390$ pc. If IRS 1 lies at the far edge of the Orion OB1 association then a larger distance $d \sim 500$ pc is possible (Sec. 1). In that case, one infers a slightly higher mass of $\sim 6 M_{\odot}$ and ZAMS spectral type of \sim B3 - B4.

The X-ray luminosity and temperature of IRS 1 are within the broad range observed in young B-type stars. The study of 20 early-type stars in the *Chandra* Orion COUP sample by Stelzer et al. (2005) included 12 B stars ranging in spectral type from B0.5 to B9. Their X-ray luminosities spanned a wide range from $\log L_X = 29.4 - 32.4$ ergs s $^{-1}$, and a hot plasma

component at typical temperatures $kT_{hot} \approx 1 - 3$ keV was present in all B-stars. Different B stars with similar spectral types showed dramatic differences in L_X and no support was found for earlier claims that L_X correlates with L_{bol} in OB stars. Using $L_{bol} = 520 L_\odot$ for IRS 1 and the range of L_X values from the different models in Table 3, we obtain $\log (L_X/L_{bol}) = -5.7 \pm 0.5$. This is consistent with values obtained for the COUP B-star sample, but some caution is needed in interpreting this ratio for IRS 1 since its L_{bol} is could be dominated by disk emission.

On the basis of the above comparisons, we conclude that a B-star classification for IRS 1 is plausible, but a mid-to-late B star is more likely than an early B star based on the luminosity determined by Butner et al. (1990). If IRS 1 is indeed an embedded intermediate-mass B-star, it is tempting to speculate that it might be a Herbig Ae/Be star progenitor. Herbig Ae/Be stars are optically-revealed intermediate-mass pre-main sequence stars which in many cases show high-temperature X-ray plasma that is likely of magnetic origin. But, the question of whether their X-ray emission is intrinsic or instead due to coronal late-type companions remains open. For previous studies of X-ray emission from Herbig Ae/Be stars, the reader is referred to Damiani et al. 1994; Zinnecker & Preibisch 1994; Preibisch & Zinnecker 1996; Skinner & Yamauchi 1996; Skinner et al. 2004; Hamaguchi, Yamauchi, & Koyama 2005; Stelzer et al. 2006, 2009; and Telleschi et al. 2007b.

5.2. X-ray Emission Processes in IRS 1

Given that the true nature of IRS 1 is not well-known and that it may be an embedded B-type star, some further discussion of the origin of its X-ray emission is warranted. Very few massive embedded stars have been detected in X-rays and little is known about their X-ray emission during early evolutionary stages prior to becoming optically visible. We thus consider several possible emission mechanisms below.

5.2.1. Shocked Winds and Outflows

The hotter plasma clearly detected at $kT_{hot} \gtrsim 2$ keV is not consistent with the cool emission ($kT \ll 1$ keV) expected from wind shocks in OB stars formed by line-driven flow instabilities (Lucy & White 1980; Lucy 1982; Feldmeier et al. 1997; Owocki et al. 1988). However, if the wind is shocking onto another object or surrounding material, or is magnetically-confined, then high-temperature plasma could be produced in a wind shock.

The predicted shock temperature for a strong adiabatic shock is $T_{shock} = 1.4 \times 10^5 \Delta v_{100}^2$ K,

or $kT_{shock} = 0.012\Delta v_{100}^2$ keV (Lamers & Cassinelli 1999). Here, Δv_{100} is the shock jump measured relative to the speed of the downstream flow, in units of 100 km s^{-1} . To achieve an X-ray temperature $kT_{shock} \sim 2$ keV, a value $\Delta v \sim 1300 \text{ km s}^{-1}$ is required. Terminal wind speeds of B5 - B9 stars are not well-determined observationally, but values $v_\infty \sim 1200 - 1400 \text{ km s}^{-1}$ are usually assumed (Cohen et al. 1997). To achieve the required velocity jump, the wind would have to be virtually stopped by dense surrounding material, e.g. either a disk, thick envelope, or close companion. The wind speed requirement could be reduced if the outflowing wind collides with a dense infalling envelope whose ram pressure exceeds that of the wind. In that case, the infalling envelope would overpower the wind, resulting in a non-stationary shock front (including both forward and reverse shocks) moving toward the star.

The above analysis can also be applied to jets and molecular outflows. High velocity wings extending out to $\approx 70 \text{ km s}^{-1}$ are visible in spectra of the $2.12 \mu\text{m}$ H_2 line toward NGC 2071-IR (Persson et al. 1981). If such an outflow shocks onto a stationary target, the maximum expected X-ray temperature is $kT_{shock} = 0.006$ keV, much too low to explain the hot X-ray plasma detected in IRS 1. As already noted (Sec. 5.1), high-velocity knots moving outward from IRS 1 at speeds up to $\sim 600 \text{ km s}^{-1}$ have been detected with the VLA (Carrasco-González et al. 2007). If such a knot shocked onto a stationary object, the maximum shock temperature would be $kT_{shock} \approx 0.4$ keV, which is again too low to explain the higher temperature plasma in IRS 1. But, this process could contribute to any cooler heavily-absorbed emission at $kT < 1$ keV.

5.2.2. Accretion Shocks

Since IRS 1 is a young class I object, it is expected to still be accreting. This is potentially relevant to the X-ray interpretation because X-rays can be produced in an accretion shock formed as infalling material impacts the (proto)star. The characteristic X-ray temperature for an accretion shock is $kT_{acc} \approx 0.02v_{100}^2$ keV, where v_{100} is the infall speed in units of 100 km s^{-1} (Ulrich 1976).

Based on the above, it is apparent that very high infall speeds $v \sim 1000 \text{ km s}^{-1}$ would be needed to produce accretion shock temperatures $kT_{acc} \sim 2$ keV, comparable to the values observed for IRS 1. To achieve such infall speeds under free-fall conditions, a massive central object equivalent to a B0V star ($M_* \sim 18 M_\odot$, $R_* \sim 7 R_\odot$; Allen 1985) would be required. But, the total luminosity of IRS 1 (Sec. 3.1) falls well short of the value $L_{bol} \sim 10^{4.4} L_\odot$ expected for a B0 ZAMS star. Thus, in the absence of any firm observational evidence for very high infall speeds toward IRS 1, it is very unlikely that the high-temperature X-ray

emission arises in an accretion shock. Any cooler plasma ($kT < 1$ keV) that might be present could be accretion-related but, as already noted, the high absorption toward IRS 1 masks such cool emission.

5.2.3. *Magnetic Activity*

Plasma temperatures $kT \gtrsim 2$ keV as seen in IRS 1 are commonly found in magnetically-active late-type stars, including T Tauri stars. The X-ray emission is accompanied by powerful magnetic reconnection flares, and is thought to arise in structures analogous to the solar corona. But, magnetic star+disk coupling undoubtedly leads to more complicated geometries in the case of TTS (reviewed by Feigelson & Montmerle 1999). Similarly, high plasma temperatures and large flares characteristic of magnetospheric processes have now been observed in low-mass class I protostars such as those in ρ Ophiuchus (Imanishi, Koyama, & Tsuboi 2001). X-ray luminosities in low-mass YSOs generally increase with stellar mass and luminosity, ranging from $L_X \sim 10^{28}$ ergs s $^{-1}$ for low masses $M_* = 0.1 - 0.2 M_\odot$ up to (and in some cases above) $L_X \sim 10^{31}$ ergs s $^{-1}$ for more massive TTS with $M_* \approx 2 M_\odot$ (Preibisch et al. 2005; Telleschi et al. 2007a).

The X-ray temperature and luminosity of IRS 1 inferred from the *Chandra* data are well within the above ranges for low-mass YSOs. It is thus possible that the X-rays observed toward IRS 1 arise in a low-mass YSO rather than a more massive object such as an embedded B-type star. The X-ray luminosity of IRS 1 could be accounted for by a TTS of mass $\sim 1 - 2 M_\odot$. Even if IRS 1 is an embedded B-type star, a late-type TTS companion could dominate the X-ray emission. Late-type companions have been proposed as a means of explaining the wide range of L_X values observed for some mid-to-late B stars in Orion with weak winds (Stelzer et al. 2005)

5.2.4. *Magnetically-Confined Wind Shocks*

If IRS 1 has an ionized wind and a sufficiently strong magnetic field, then the B field can confine the wind into two oppositely directed streams in each hemisphere which collide near the magnetic equator, forming a magnetically-confined wind shock (MCWS). Such a shock can reach X-ray emitting temperatures. The MCWS mechanism has been used to explain high-temperature X-ray emission in magnetic Ap-Bp stars (Babel & Montmerle 1997a) and young magnetic O stars such as θ^1 Ori C (Babel & Montmerle 1997b; Gagné et al. 2005).

The radio properties of IRS 1 do suggest it has an ionized wind or jet (Carrasco-

Gonzalez et al. 2007), but there are so far no reports of a magnetic field. Even so, an estimate of the field strength needed to confine the wind can be obtained by making reasonable approximations under the assumption that it is a mid-to-late B star.

The maximum X-ray temperature for a MCWS is given by the adiabatic shock equation (Sec. 5.2.1). We thus assume a terminal wind speed $v_\infty \sim 1300 \text{ km s}^{-1}$ for IRS 1 to achieve a shock temperature comparable to the observed value ($kT_{shock} \sim 2 \text{ keV}$). The degree to which the wind is confined by the magnetic field is expressed in terms of the confinement parameter $\eta = B^2 R_*^2 / \dot{M} v_\infty$ where B is the equatorial magnetic field strength (ud-Doula & Owocki 2002). For values of $\eta \approx 1$ (critical confinement), the B field is able to confine the wind. For a B5V star ($R_* \approx 3.8 R_\odot$, Allen 1985), the above relation with $\eta = 1$ becomes $B_{100}^2 \approx 47 \eta \dot{M}_{-6}$, where B_{100} is in units of 100 G and \dot{M}_{-6} is in units of $10^{-6} M_\odot \text{ yr}^{-1}$. The mass-loss rates of mid-to-late B stars are not well-determined empirically, but $B \sim 2 \text{ G}$ for $\dot{M} = 10^{-11} M_\odot \text{ yr}^{-1}$ (Cohen et al. 1997) and $B \sim 70 \text{ G}$ for $\dot{M} = 10^{-8} M_\odot \text{ yr}^{-1}$. The latter \dot{M} values are typical of intermediate mass Herbig Ae/Be stars (Skinner et al. 1993).

In summary, the MCWS mechanism is a potential means of explaining the high-temperature plasma in IRS 1. But, without a magnetic field detection and specific estimates of B-field strength and mass-loss parameters, any more definitive comparisons against MCWS model predictions cannot be made.

5.2.5. Summary of Emission Mechanisms

Based on the above discussion, we conclude that the high-temperature plasma at $kT \sim 2 \text{ keV}$ in IRS 1 is most likely due to either a high-speed wind ($v_\infty \gtrsim 1200 \text{ km s}^{-1}$) shocking onto a dense target (e.g. a disk or dense surrounding envelope), or it originates in a low-mass magnetically-active YSO companion. The wind-shock interpretation is plausible if IRS 1 is an embedded B-type star whose wind has already turned on, and the extended bright radio continuum emission detected with the *VLA* does point to an early-type star with a strong wind or jet. We cannot rule out a magnetically-confined wind shock, but there are insufficient observational constraints on magnetic field strength and wind parameters to rigorously test MCWS models. Even if IRS 1 is an embedded B-type star (which seems likely), a lower mass YSO companion at close separation could still be responsible for some (or even all) of the observed X-ray emission. The X-ray luminosity determined from spectral models of IRS 1 is at the high end of the range observed for low-mass YSOs. If the X-ray emission is due entirely to a T Tauri-like companion, then the known correlation between L_X and stellar mass suggests a companion mass in excess of $1 M_\odot$.

5.3. Fluorescent Iron Emission in IRS 1

A fluorescent Fe line at 6.4 keV can be produced by photoionization when “cold” material containing neutral or weakly-ionized iron is irradiated by a nearby hard X-ray continuum source. Photons with energies above 7.11 keV are needed to eject a K-shell electron. The K-shell vacancy is filled by another electron such as an L-shell electron, resulting in fluorescent Fe line emission at 6.4 keV. The line is in fact a doublet consisting of two closely-spaced lines at 6.391 keV and 6.404 keV, but these cannot be distinguished at the energy resolution of the ACIS-I CCDs. The above photoionization process is discussed in more detail by George & Fabian (1991) and Kallman et al. (2004). Analysis of the fluorescent Fe line can potentially provide information on the properties of the absorber and its location relative to the hard continuum source.

The fluorescent Fe line detected in IRS 1 is faint (Fig. 11), consisting of 7 events distributed in the 6.298 - 6.536 keV energy range, with a median energy 6.395 keV and mean energy 6.419 keV. Three of the seven photons arrived in the first half of the observation. A KS test applied to the arrival times of the 7 events shows no significant variability and gives a probability of constant count rate $P_{const} = 0.35$. The line flux is $7.2 (\pm 1.2) \times 10^{-15}$ ergs $\text{cm}^{-2} \text{s}^{-1}$. This is about a factor of five less than measured during the March 2005 *XMM* observation (S07). The line equivalent width in the ACIS-I spectrum is uncertain because the continuum flux near 6.4 keV is very faint. But, our flux estimates give values $EW \geq 2.4$ keV, consistent with the previous *XMM* estimate (S07).

The detection of fluorescent Fe line emission in IRS 1 is a rare occurrence in YSOs, but certainly not unique. Tsujimoto et al. (2005) examined 1616 X-ray sources detected in the deep *Chandra* COUP observation of the Orion Nebula Cluster and identified seven sources with excess emission at 6.4 keV and line equivalent widths $EW \leq 0.27$ keV. All seven X-ray sources showed flare-like variability and high line-of-sight absorption $N_H \gtrsim 10^{22} \text{ cm}^{-2}$, as also seen in IRS 1. The broad fluorescent Fe line during a superhot flare in V1486 Ori (COUP source 331) was analyzed by Czesla & Schmitt (2007). The 6.4 keV line has also been detected in other YSOs including the class I objects YLW 16A (Imanishi et al. 2001) and Elias 29 (Giardino et al. 2007) in ρ Oph, and the class I source R CrA X_E (= IRS 7B; Hamaguchi et al. 2005).

The fluorescent Fe line detection in IRS 1 is interesting in three respects: (i) it was detected in the apparent absence of any large-amplitude flares (but low-level variability may be present), (ii) there is no accompanying line at 6.7 keV from the highly-ionized Fe XXV complex, and (iii) the line has a very large equivalent width that is difficult to account for by illuminated disk models.

The absence of any detectable large flares in IRS 1 is unusual because the fluorescent Fe lines in almost all of the YSOs mentioned above occurred during flares. Analysis of the V1486 Ori data showed that its broad fluorescent Fe line appeared during the rise phase of a flare (Czesla & Schmitt 2007). An interesting exception is Elias 29, which showed a 6.4 keV line during a large flare. But the line persisted after the flare had decayed, remaining over a timescale much longer than the radiative lifetimes of fluorescent Fe transitions. Giardino et al. (2007) thus concluded that the X-ray flare was not directly responsible for the post-flare 6.4 keV line. Instead, they proposed that the line was produced by collisional ionization from an unseen population of nonthermal electrons.

The 6.4 keV line in IRS 1 is similar to Elias 29 in the sense that it does not appear to be directly associated with a large flare. The line was present in both the *XMM-Newton* spectrum obtained in March 2005 and in the more recent *Chandra* spectrum, but no large flare was detected in either observation. If a large flare was involved, then it must have occurred prior to the start of the observations, or it escaped detection (as could occur if the flare occurred on the back side of IRS 1 and was occulted).

Unless large X-ray flares occurred and escaped detection, the existing data indicate that the 6.4 keV line in IRS 1 is persistent and does not correlate with large flares. In that case, some mechanism needs to be operating nearly continuously to ionize the absorbing material. At present, the ionizing source and the ionization mechanism are not known. The obvious candidate for the ionizing source is IRS 1 itself. But, in terms of hardness, its *Chandra* spectrum is rather benign, showing no large flares, no Fe XXV line and a weak continuum above ~ 7 keV. However, we cannot rule out the possibility of substantial hard emission ($kT \gtrsim 20$ keV) above the energy range accessible to *Chandra* and *XMM*. Nevertheless, the intriguing possibility does remain that the hard ionizing source is not IRS 1 and is not directly detected in our X-ray observations.

However, before discounting IRS 1 as the ionizing source, two factors should be noted. First, low-level variations appear to be present in the *Chandra* light curve of IRS 1 (Fig. 9). These variations may be a signature of persistent low-level flaring. If that is the case, then quasi-continuous hard energy release by repeated small flares may play a role in photoionizing the absorber. Second, IRS 1 is thought to drive a powerful outflow and also shows evidence of a radio jet (Carrasco-González et al. 2007). If a population of nonthermal electrons is produced in the shocked jet (which may be magnetically collimated) they could play a role in collisional ionization of the absorber. Collisional ionization has been invoked as a means of explaining the 6.4 keV line in Elias 29 (Giardino et al. 2007) and in the active binary system II Peg (Osten et al. 2007). If a population of nonthermal particles is present, they *may* imprint a signature on the radio continuum emission. Thus, further radio observations of

IRS 1 at lower frequencies where nonthermal emission can dominate over thermal (free-free) emission could be informative.

The large equivalent width $EW \geq 2.4$ keV of the IRS 1 fluorescent line is a noteworthy feature of its X-ray spectrum. This value is extreme for a YSO, exceeding even the maximum value $EW = 1.4$ keV observed for V1486 Ori during the rise phase of its superhot flare (Czesla & Schmitt 2007). These values conflict with theoretical models of centrally illuminated cold disks, which predict $EW \approx 0.1 - 0.2$ keV (George & Fabian 1991). The EW of the 6.4 keV line is proportional to the column density $N_{H'}$ in the fluorescing material (Tsujiimoto et al. 2005). If taken literally, the large EW of IRS 1 would imply a high absorber column density $N_{H'} \gtrsim 10^{24} \text{ cm}^{-2}$ (S07). Since this value is much larger than the line-of-sight photoelectric absorption inferred from the X-ray spectrum (Table 3), one is led to the conclusion that the fluorescing material lies off the line-of-sight. But, the above conclusion rests on the assumption that the continuum measured in the X-ray spectrum has undergone negligible absorption. If the hard irradiating source is not IRS 1 itself and is occulted or very heavily absorbed, then some or all of the intrinsic hard continuum will be missing from the observed X-ray spectrum. In that case, the EW measurement would be based on a depressed continuum and thus overestimated, along with $N_{H'}$.

In summary, our main conclusions with respect to the fluorescent Fe line in IRS 1 are: (i) the line is present even in the absence of the Fe XXV line (6.67 keV) and any large flare detections, and evidently does not directly depend on large-amplitude X-ray flares for its existence, (ii) the line flux is variable, showing a decrease between the *XMM* and *Chandra* observations taken 2.6 years apart, but no significant variability during the 67 ksec *Chandra* observation, (iii) the line EW is much larger than predicted by centrally-illuminated disk models, suggesting either that the photoionization models do not accurately reflect the line formation process and that other mechanisms (e.g. collisional ionization) could play a role, or that the observed continuum is not the same as the intrinsic continuum of the photoionizing source (e.g. due to the effects of absorption or occultation), and (iv) the hard ionizing source may have so far escaped X-ray detection.

6. Conclusions

The main conclusions of this study are the following:

1. *Chandra*'s excellent spatial resolution has resolved the NGC 2071-IR core region into six X-ray sources. X-ray emission was detected at or near the infrared sources IRS 1,2,3,4 and 6 and the radio source VLA 1. X-ray analysis shows that these sources

are viewed through moderate-to-high absorption and have hard/high-temperature X-ray emission ($kT \gtrsim 2$ keV), consistent with their classification as embedded young stars. In some cases such as IRS 3, the X-ray position is significantly offset from the near-IR position, supporting the conclusion that the near-IR peak traces nebulosity or scattered light and not the star itself.

2. *Spitzer* IRAC detections of IRS 1,2,4,6, and 7 provide the first reliable mid-IR colors for these objects. Using IRAC colors along with near-IR colors based on published JHK_s photometry and the sharply-rising IR SED, we conclude that IRS 1 is a class I protostar. IRS 2 and IRS 7 are also likely class I protostars, but could be heavily-reddened class II objects. IRS 4 and IRS 6 have colors consistent with reddened class II objects. No reliable IRAC photometry or mid-IR colors were obtained for IRS 3, 5, 8, or 8a, but near-IR colors determined from existing JHK_s photometry show that these objects are heavily-reddened.
3. *Chandra* provides the first X-ray detection of VLA 1, and its X-ray emission is likely variable. X-ray spectral models require a strong absorption component for VLA 1, equivalent to $A_V = 39$ [22 - 69] mag. Thus, VLA 1 appears to be more heavily-embedded than IRS 1 and it could thus be an even younger, less-evolved object. There are as yet no IR data for VLA 1 on which to base a YSO classification.
4. The existing data for IRS 1 are consistent with a mid-to-late B (proto)star classification. The X-ray spectrum of IRS 1 is heavily-absorbed below 1 keV and clearly reveals high-temperature plasma at $kT \sim 2 - 3$ keV. Such plasma could originate either in a shocked high-velocity wind/jet or in a magnetically-active low-mass YSO companion.
5. The most important finding of this study is that the fluorescent Fe line in IRS 1 is persistent and present even in the absence of large flares. Thus, an as yet unidentified quasi-continuous process that operates independently of large flares is needed to explain the K-shell ionization of cold proximate material that leads to formation of fluorescent Fe. Both the *Chandra* and *XMM-Newton* light curves show signs of low-level variability, suggesting that short bursts of hard emission from persistent low-level flaring could play a role in ionizing the absorber. The large equivalent width $EW \geq 2.4$ keV of the 6.4 keV line is noteworthy because it is well in excess of values predicted by centrally illuminated disks models. Large 6.4 keV line equivalent widths have also been noted in other YSOs such as V1486 Ori. If interpreted literally, the large EW values imply either a very high absorption column density in the cold absorber, or perhaps processes other than photoionization (e.g. collisional ionization in shocks). However, some caution is needed in interpreting the large EW for IRS 1, since the absence of large flares raises the possibility that it is not the hard ionizing source. If the ionizing source is occulted

by IRS 1 or buried behind heavy absorption, then the hard continuum measured in the IRS 1 spectrum may be less than the intrinsic continuum of the ionizing source (“missing continuum”), leading to an overestimate of the equivalent width.

S.S., K.F., and M.M. acknowledge *Chandra* support from SAO grant GO7-8008A. M.A. acknowledges support from a Swiss National Science Foundation Professorship (PP002–110504). We have utilized data products from the Two Micron All-Sky Survey (2MASS), which is a joint project of the University of Massachusetts and IPAC/CalTech. This work is based in part on data obtained with the *Spitzer* Space Telescope, which is operated by the Jet Propulsion Laboratory, CalTech, under a contract with NASA. We would like to thank C. Carrasco-González and G. Sandell for radio positions and J. Hong for information on quartile analysis computer codes.

REFERENCES

- Allen, C.W. 1985, *Astrophysical Quantities* (London: Athlone)
- Allen, L.E. et al. 2004, *ApJ*, 154, 363
- Allen, L.E. et al. 2007, in *Protostars and Planets V*, eds. B. Reipurth, D. Jewitt, & K. Keil (Tucson: U. of Arizona Press), 361
- Anders, E. & Grevesse, N. 1989, *Geochim. Cosmochim. Acta*, 53, 197
- Anthony-Twarog, B. 1982, *AJ*, 87, 1213
- Aspin, C., Sandell, G., & Walther, D.M. 1992, *MNRAS*, 258, 684
- Babel, J. & Montmerle, T. 1997a, *A&A*, 323, 121
- Babel, J. & Montmerle, T. 1997b, *A&A*, 485, L29
- Bally, J. 1982, *ApJ*, 261, 558
- Bessell, M.A. & Brett, J.M. 1988, *PASP*, 100, 1134
- Brandt, W.N. et al. 2001, *AJ*, 122, 2810
- Brown, A.G.A., de Geus, E.J., & de Zeeuw, P.T. 1994, *A&A*, 289, 101
- Butner, H.M., Evans, N.J., Harvey, P.M., Mundy, L.G., Natta, A., & Randich, M.S. 1990, *ApJ*, 364, 164
- Carpenter, J.M. 2001, *AJ*, 121, 2851
- Cash, W. 1979, *ApJ*, 228, 939
- Carrasco-González, C., Anglada, G., Rodríguez, L.F., Gómez, J.F., Torrelles, J.M., & Osorio, M. 2007, in *Massive Star Formation: Observations Confront Theory* (Heidelberg, Germany), <http://www.mpia.de/MSF07/>
- Cohen, D.H., Cassinelli, J.P., & MacFarlane, J.J. 1997, *ApJ*, 487, 867
- Cohen, J.G., Persson, S.E., Elias, J.H., & Frogel, J.A. 1981, *ApJ*, 249, 481
- Czesla, S. & Schmitt, J.H.M.M. 2007, *A&A*, 470, L13
- Damiani, F., Micela, G., Sciortino, S., & Harnden, F.R. 1994, *ApJ*, 436, 807

- Eislöffel, J. 2000, *A&A*, 354, 236
- Fazio, G.G. et al. 2004, *ApJS*, 154, 10
- Feigelson, E.D. & Montmerle, T. 1999, *ARA&A*, 37, 363
- Feldmeier, A., Kudritzki, R.-P., Palsa, R. Pauldrach, A.W.A., & Puls, J. 1997, *A&A*, 320, 899
- Flaherty, K.M., & Muzerolle, J. 2008, *AJ*, 135, 966
- Gagné, M. et al. 2005, *ApJ*, 628, 986
- George, I.M. & Fabian, A.C. 1991, *MNRAS*, 249, 352
- Getman, K.V. et al. 2005, *ApJS*, 160, 319
- Giardino, G., Favata, F., Pillitteri, I., Flaccomio, E., Micela, G., & Sciortino, S. 2007, *A&A*, 475, 891
- Gibb, A.G. 2008, in *Handbook of Star Forming Regions, Volume 1, The Northern Sky*, ed. B. Reipurth (San Francisco: ASP), 693
- Gorenstein, P. 1975, *ApJ*, 198, 95
- Gutermuth, R.A. et al. 2004, *ApJS*, 154, 374
- Gutermuth, R.A. et al. 2008, *ApJ*, 674, 336
- Hamaguchi, K. et al. 2005, *ApJ*, 623, 291
- Hamaguchi, K., Yamauchi, S., & Koyama, K. 2005, *ApJ*, 618, 360
- Hartmann, L. et al. 2005, *ApJ*, 629, 881
- Harvey, P.M., Campbell, M.F., Hoffmann, W.F., Thronson, H.A., & Gatley, I. 1979, *ApJ*, 229, 990
- Hong, J., Schlegel, E.M., & Grindlay, J.E. 2004, *ApJ*, 614, 508
- Imanishi, K., Koyama, K., & Tsuboi, Y. 2001, *ApJ*, 557, 747
- Johansson, L.E.B., Höglund, B., Winnberg, A., Rieu, N.Q., & Goss, W.M. 1974, *ApJ*, 189, 455

- Kallman, T.R., Palmeri, P., Bautista, M.A., Mendoza, C., & Krolik, J.H. 2004, *ApJS*, 155, 675
- Lada, E.A., DePoy, D.L., Evans, N.J., & Gatley, I. 1991, *ApJ*, 371, 171
- Lamers, H.J.G.L.M. & Cassinelli, J.P. 1999, *Introduction to Stellar Winds* (Cambridge: Cambridge U. Press), 360
- Landsman, W.B. 1993, in *Astronomical Data Analysis and Software Systems II*, A.S.P. Conf. Series vol. 52, eds. R.J. Hanisch, R.J.V. Brissenden, & J. Barnes, 246
- Lucy, L.B. 1982, *ApJ*, 255, 286
- Lucy, L.B. & White, R.L. 1980, *ApJ*, 241, 300
- Lynds, B.T. 1962, *ApJS*, 7, 1
- Maddalena, R.J., Morris, M., Moscowitz, J., & Thaddeus, P. 1986, *ApJ*, 303, 375
- Megeath, S.T. et al. 2005a, in *Massive Star Birth: A Crossroads of Astrophysics*, Proc. IAU Symp. 227, eds. R. Cesaroni, M. Felli, E. Churchwell, & M. Walmsley (Cambridge: Cambridge U. Press), 383
- Megeath, S.T., Allgaier, E., Young, E., Allen, T., Pipher, J.L., & Wilson, T.L. 2009, *AJ*, 137, 4072
- Megeath, S.T., Hartmann, L., Luhman, K.L., & Fazio, G.G. 2005b, *ApJ*, 634, L113
- Meyer, M.R., Calvet, N., & Hillenbrand, L.A. 1997, *AJ*, 114, 288
- Moretti, A., Campana, S., Lazzati, D., & Tagliaferri, G. 2003, *ApJ*, 588, 696
- Osten, R.A., Drake, S., Tueller, J., Cummings, J., Perri, M., Moretti, A., & Covino, S. 2007, *ApJ*, 654, 1052
- Owocki, S.P., Castor, J.I., & Rybicki, G.B. 1988, *ApJ*, 335, 914
- Pankonin, V., Winnberg, A., & Booth, R.S. 1977, *A&A*, 58, L25
- Persson, S.E., Geballe, T.R., Simon, T., Lonsdale, C.J., & Baas, F. 1981, *ApJ*, 251, L85
- Preibisch, T. et al. 2005, *ApJS*, 160, 401 (P05)
- Preibisch, T. & Zinnecker, H. 1996, in *Röntgenstrahlung from the Universe*, ed. H. Zimmerman & J. Trümper (Garching: MPE), 17

- Press, W.H., Teukolsky, S.A., Vetterling, W.T., & Flannery, B.P. 1992, *Numerical Recipes in FORTRAN: The Art of Scientific Computing* (2nd ed.; New York: Cambridge Univ. Press), 617
- Sandell, G., Nyman, L.A., Haschick, A., & Winnberg, A. 1985, in *Lecture Notes in Physics*, 237, *Nearby Molecular Clouds*, eds. H. Araki et al. (Berlin:Springer-Verlag, 234
- Sandell, G.H.L., Wright, M., Goss, W., & Corder, S. 2009, *BAAS*, 41(No. 1), 460
- Siess, L., Dufour, E., & Forestini, M. 2000, *A&A*, 358, 593
- Skinner, S.L., Brown, A., & Stewart, R.T. 1993, *ApJS*, 87, 217
- Skinner, S.L., Güdel, M., Audard, M., & Smith, K. 2004, *ApJ*, 614, 221
- Skinner, S.L., Simmons, A.E., Audard, M., & Güdel, M. 2007, *ApJ*, 658, 1144 (S07)
- Skinner, S.L. & Yamauchi, S. 1996, *ApJ*, 471, 987
- Snell, R.L. & Bally, J. 1986, *ApJ*, 303, 683
- Snell, R.L., Scoville, N.Z., Sanders, D.B., & Erikson, N.R. 1984, *ApJ*, 284, 176
- Stelzer, B. et al. 2005, *ApJS*, 160, 557
- Stelzer, B., Micela, G., Hamaguchi, K., & Schmitt, J.H.M.M. 2006, *A&A*, 457, 223
- Stelzer, B., Robrade, J., Schmitt, J.H.M.M., & Bouvier, J. 2009, *A&A*, 493, 1109
- Stojimirović, I., Snell, R. L., & Narayanan, G. 2008, *ApJ*, 679, 557
- Strom, K.M., Strom, S.E., Carrasco, L., & Vrba, F.J. 1975, *ApJ*, 196
- Strom, K.M., Strom, S.E., & Vrba, F.J. 1976, *AJ*, 81, 308
- Tamura, M. et al., 2007, *PASJ*, 59, 467 (T07)
- Telleschi, A., Güdel, M., Briggs, K.R., Audard, M., & Palla, F. 2007a, *A&A*, 468, 425
- Telleschi, A., Güdel, M., Briggs, K.R., Skinner, S.L., Audard, M., & Franciosini, E. 2007b, *A&A*, 468, 541
- Thompson, R.I. 1984, *ApJ*, 283, 165
- Torrelles, J.M., Gómez, J.F., Rodríguez, L.F., Curiel, S., Anglada, G., & Ho, P.T.P. 1998, *ApJ*, 505, 756

- Tsujimoto, M. et al. 2005, ApJS, 160, 503
- ud-Doula, A. & Owocki, S.P. 2002, ApJ, 576, 413
- Ulrich, R.K. 1976, ApJ, 210, 377
- Vuong, M.H., Montmerle, T., Grosso, N., Feigelson, E.D., Verstraete, L., & Ozawa, H. 2003, A&A, 408, 581
- Walther, D.M., Geballe, T.R., & Robson, E.I. 1991, ApJ, 377, 246
- Walther, D.M., Robson, E.I., Aspin, C., & Dent, W.R.F. 1993, ApJ, 418, 310 (W93)
- Wilson, B.A., Dame, T.M., Masheder, M.R.W., & Thaddeus, P. 2005, A&A, 430, 523
- Winston, E. et al. 2007, ApJ, 669, 493
- Zhao, B. et al. 1999, AJ, 118, 1347
- Zhou, S., Evans, N.J., & Mundy, L.G. 1990, ApJ, 355, 159
- Zinnecker, H. & Preibisch, T., 1994, A&A, 292, 152

Table 1. X-ray Sources Near NGC 2071-IRS 1^a

Name	R.A. (J2000)	Decl. (J2000)	Net Counts (cts)	E ₂₅ , E ₅₀ , E ₇₅ (keV)	P _{const}	K _s (mag)	Identification(offset) (arcsec)
IRS 3 ^b	05 47 04.63	+00 21 48.0	18±4	3.68, 4.52, 6.06	0.76	12.18 ^c	VLA J054704.62+002147.8 (0.25) ^d
IRS 1	05 47 04.75	+00 21 42.9	144±12	1.79, 2.22, 3.27	0.11	11.21	2M J05470477+0021428 (0.42)
VLA 1	05 47 04.77	+00 21 45.1	90±10(v)	2.98, 3.52, 4.48	0.02	...	VLA J054704.758+002145.50 (0.44) ^e
IRS 4	05 47 05.10	+00 22 01.6	11±3	1.18, 1.75, 2.53	0.14	10.86	2M J05470512+0022013 (0.48)
IRS 2	05 47 05.35	+00 21 50.4	4±1 ^f	... , 5.22, ^f	10.41	2M J05470538+0021500 (0.66) ^e
IRS 6	05 47 05.60	+00 22 11.1	48±7(v)	1.56, 2.05, 3.21	0.01	10.10	2M J05470570+0022103 (1.68) ^g

^aNotes: *Chandra* X-ray data are from CCD3 (ACIS chip I3) using events in the 0.3-7 keV range. Tabulated quantities are: source name, J2000.0 X-ray position (R.A., Decl.), net counts and net counts error from *wavdetect* (accumulated in a 67,180 s exposure, rounded to the nearest integer, background subtracted and PSF-corrected), 25%, 50% (median), and 75% photon quartile energies E₂₅, E₅₀, and E₇₅, K_s magnitude of near-IR 2MASS counterpart, and 2MASS (2M) or radio (VLA) candidate counterpart identification within a 2'' search radius. The offset (in arcsecs) between the X-ray and counterpart position is given in parentheses. A (v) following Net Counts error indicates that the source is likely variable as indicated by a variability probability P_{var} ≥ 0.95 determined from the Kolmogorov-Smirnov (KS) statistic.

^bThe name IRS 3 corresponds to the infrared source identified by W93, which lies ≈2.3'' northeast of the X-ray source.

^cThe IRS 3 K magnitude is from W93.

^dThe closest 2MASS source (2M J05470473+0021497) lies at an offset of 2.34'' and K_s = 12.88. A *Spitzer* IRAC source is visible and the 4.5 μm IRAC position gives an offset of ≈0.42'' from the *Chandra* position.

^eThe X-ray source is offset by 0.27'' from radio source VLA J054705.367+002150.51. VLA coordinates are from C. Carrasco-González 2009 (private communication).

^fFaint source not found by *wavdetect*. Net counts are measured within an extraction circle of radius 1''. Insufficient counts for variability analysis or calculation of reliable E₂₅ and E₇₅ values.

^gA *Spitzer* IRAC source is visible and the 3.6 μm position gives an offset of ≈1.19'' from the *Chandra* position.

Table 2. Spitzer IRAC Photometry: NGC 2071-IR^a

Object	[3.6] (mag)	[4.5] (mag)	[5.8] (mag)	[8.0] (mag)
IRS 1	8.359 ± 0.005	6.246 ± 0.005	4.576 ± 0.003	2.819 ± 0.001
IRS 2	7.747 ± 0.046	6.382 ± 0.008	5.581 ± 0.005	4.717 ± 0.005
IRS 3	...	7.250 ± 0.015
IRS 4	9.418 ± 0.035	8.263 ± 0.007	7.776 ± 0.005	6.678 ± 0.007
IRS 5 ^b
IRS 6	8.609 ± 0.023	8.052 ± 0.003	7.619 ± 0.003	6.966 ± 0.006
IRS 7 ^c	8.546 ± 0.051	6.705 ± 0.003	5.776 ± 0.002	4.654 ± 0.002
IRS 8 ^d	>11.35

^aIRAC magnitudes were derived using a circular aperture of radius $r = 2$ pixels and a background annulus $r = 2 - 6$ pixels (pixel size $\approx 1.22''$). The given magnitudes are background-subtracted and aperture-corrected. Aperture correction factors are: 1.213 ($3.6 \mu\text{m}$), 1.234 ($4.5 \mu\text{m}$), 1.379 ($5.8 \mu\text{m}$), 1.584 ($8.0 \mu\text{m}$). Magnitude zero points (Z_0) for count rate units of DN s^{-1} are: 19.6642 ($3.6 \mu\text{m}$), 18.9276 ($4.5 \mu\text{m}$), 16.8468 ($5.8 \mu\text{m}$), 17.3909 ($8.0 \mu\text{m}$), where $[\text{mag}] = -2.5 \log_{10}(\text{DN s}^{-1}) + Z_0$. Magnitude uncertainties are formal uncertainties (internal errors only). The actual uncertainties will in general be larger than the quoted values due to systematic effects such as zero point uncertainties and other factors which can affect measurement accuracy such as bright nearby nebulosity.

^bNo photometry measured. IRS 5 is located between the nearby bright sources IRS 1 and IRS 2 and is not clearly visible in IRAC images.

^cThe MIPS $24 \mu\text{m}$ data for IRS 7 give a magnitude $0.71 \pm 0.03 \text{ mag}$.

^dSource appears nebulous and is extended in NE/SW direction. Possibly a close pair. Photometry is uncertain and the lower limit is based on counts inside a $r = 2$ pixel extraction circle with no background subtraction, centered at J054704.28+002137.9.

Table 3. *Chandra* Spectral Fit Results

Parameter				
Object	IRS 1	IRS 1	VLA 1	IRS 6
Model	2T APEC ^a	VPSHOCK ^a	1T APEC	1T APEC ^b
N _H (10 ²² cm ⁻²)	3.62 [2.75 - 4.52]	3.03 [2.20 - 4.52]	8.68 [4.88 - 15.3]	1.24 [0.37 - 2.31]
kT ₁ (keV)	{0.55} ^c	2.31 [1.31 - 5.99]	2.22 [1.00 - 7.18]	3.85 [1.47 - ...]
norm ₁ (10 ⁻⁴)	2.60 [0.38 - 5.03]	0.46 [0.23 - 0.82]	1.18 [0.95 - 1.39]	0.31 [0.17 - 0.65]
kT ₂ (keV)	3.31 [1.51 - 21.4]
norm ₂ (10 ⁻⁵)	2.82 [1.07 - 5.31]
E _{line} (keV)	{6.40}	{6.40}
σ _{line} (keV)	{0.05}	{0.05}
norm _{line} (10 ⁻⁷)	6.89 [1.49 - 12.0]	7.10 [2.43 - 12.5]
Abundances	solar ^d	solar ^e	solar	solar
χ ² /dof	8.10/8	9.3/8	2.13/5	1.26/3
χ _{red} ²	1.01	1.16	0.43	0.42
F _X (10 ⁻¹⁴ ergs cm ⁻² s ⁻¹)	2.99 (66.8)	2.84 (24.2)	2.54 (15.7)	2.65 (4.71)
F _{X,line} (10 ⁻¹⁵ ergs cm ⁻² s ⁻¹)	7.01 (7.01)	8.04 (8.04)
log L _X (ergs s ⁻¹)	31.08	30.64	30.45	29.93

Note. — Based on fits of binned ACIS spectra using XSPEC v12.4.0. The spectra were rebinned to a minimum of 10 counts per bin. The tabulated parameters are absorption column density (N_H), plasma temperature (kT), XSPEC normalization (norm), Gaussian line centroid energy (E_{line}), line width (σ_{line} = FWHM/2.35), line normalization (norm_{line}). For the APEC model, the XSPEC norm is related to the emission measure (EM) by EM = 4π10¹⁴d_{cm}²×norm, where d_{cm} is the stellar distance in cm. Quantities enclosed in curly braces were held fixed during fitting. Solar abundances are referenced to Anders & Grevesse (1989). Square brackets enclose 90% confidence intervals and an ellipsis means that the algorithm used to compute the confidence bound did not converge. X-ray flux (F_X) is the observed (absorbed) value followed in parentheses by the unabsorbed value in the 0.5 - 7.5 keV range. The continuum-subtracted Gaussian line flux (F_{X,line}) is measured in the 6.2 - 6.6 keV range. X-ray luminosity (L_X) is the unabsorbed value in the 0.5 - 7.5 keV range. A distance of 390 pc is assumed.

^aA fixed-width Gaussian line at 6.4 keV was included in the fit to model the faint fluorescent Fe emission.

^bDue to low counts, the spectrum was binned to a minimum of 8 counts per bin.

^cThe value of kT₁ is not tightly constrained. Values in the range kT₁ = 0.25 - 0.70 keV give nearly identical χ² and lower values of kT₁ converge to higher N_H.

^dThe solar abundance 2T APEC fit can be improved by allowing the Si abundance to vary. This yields kT₁ = [0.55] keV (held fixed), N_H = 2.49 [1.44 - 3.73] × 10²² cm⁻², norm₁ = 3.04 [2.66 - 16.3] × 10⁻⁵, kT₂ = 2.55 [1.53 - 7.06] keV norm₂ = 3.42 [2.01 - 5.62] × 10⁻⁵, Si = 5.1 [1.4 - 19.] × solar, χ²/dof = 4.94/7, and log L_X = 30.40 ergs s⁻¹.

^eThe solar abundance VPSHOCK fit can be improved by allowing the Si abundance to vary. This yields kT₁ = 3.27 [1.43 - 12.0] keV, N_H = 2.68 [1.20 - 3.66] × 10²² cm⁻², norm₁ = 2.92 [1.23 - 5.44] × 10⁻⁵, Si = 2.2 [1.0 - 13.9] × solar, χ²/dof = 6.33/7, and log L_X = 30.44 ergs s⁻¹.

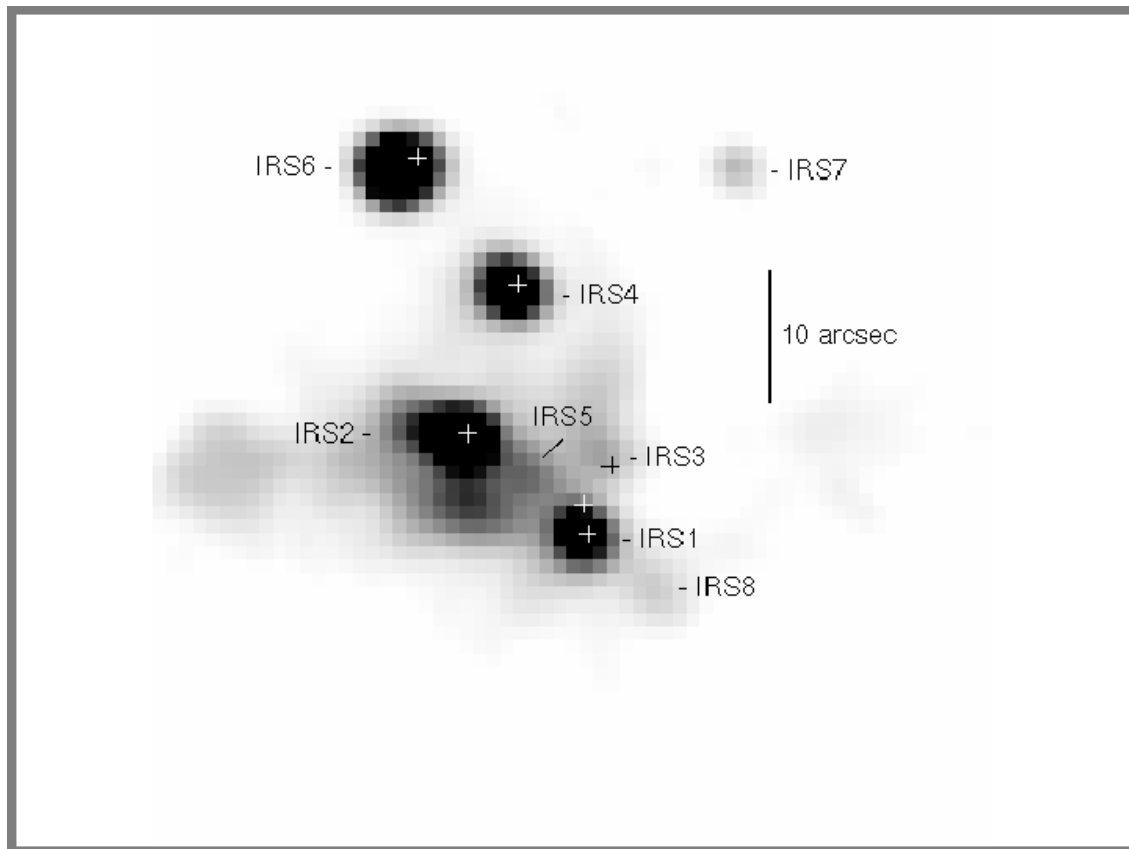


Fig. 1.— A 2MASS K_s-band ($2.16 \mu\text{m}$) image of the region near IRS 1. Crosses mark positions of Chandra X-ray sources. Significant offsets between Chandra and 2MASS positions exist for IRS 3 ($2.''3$) and IRS 6 ($1.''7$). See Table 1 for positions. No X-ray emission was detected by Chandra at the 2MASS positions of IRS 5, IRS 7, and IRS 8. Log intensity scale. North is up, east is left.

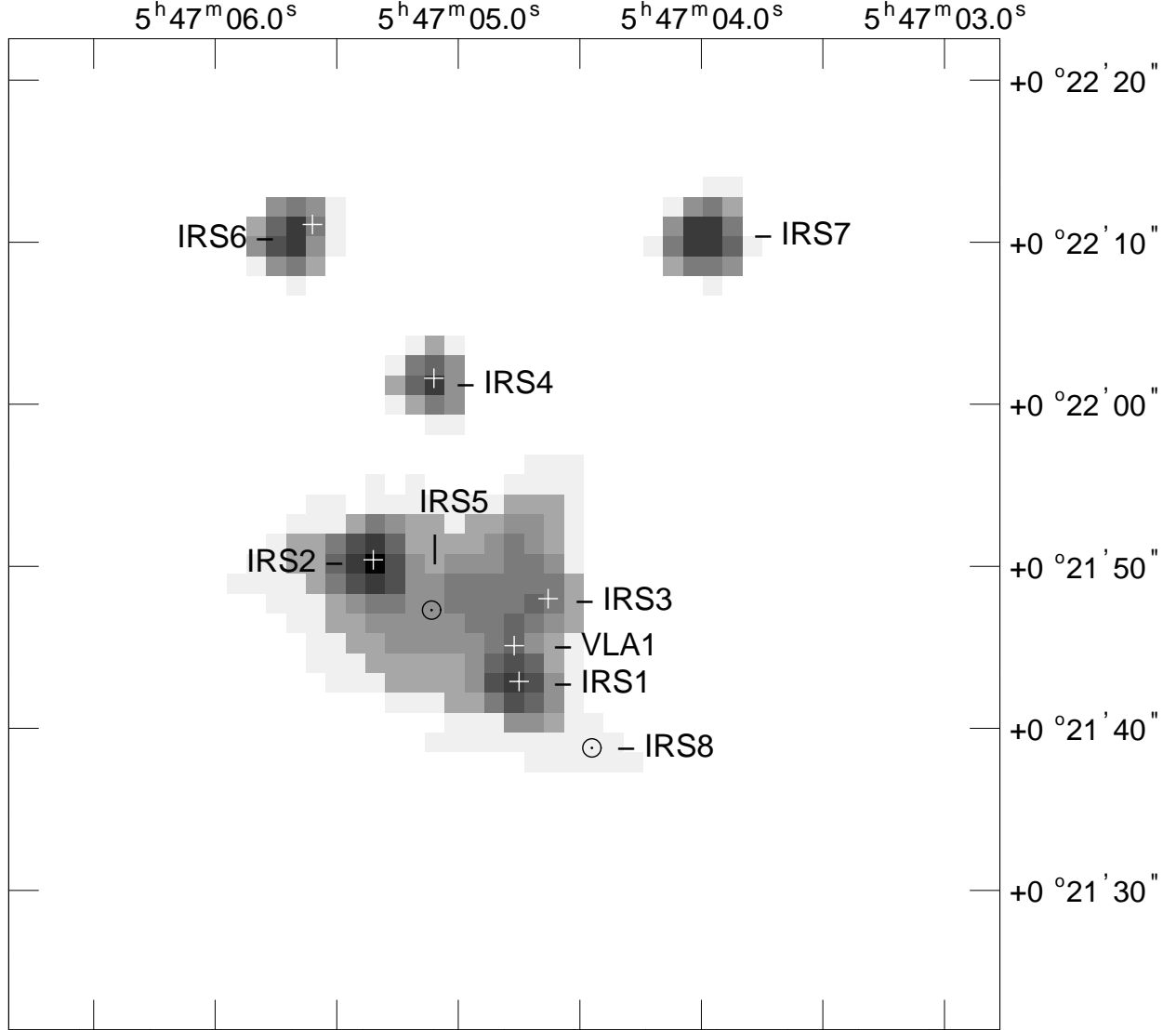


Fig. 2.— An unsaturated Spitzer IRAC 3.6 μm (ch1) image of the region near IRS 1 (program 043). The image is a single 0.6 s frame. Crosses mark positions of Chandra X-ray sources. The positional offset between Chandra and IRAC for IRS 3 is only 0."42, in better agreement than obtained with 2MASS (Fig. 1). The positional offset between Chandra and IRAC for the binary system IRS 6 is 1."2, again better than obtained with 2MASS (Fig. 1). IRS 5, IRS 7, and IRS 8 were not detected by Chandra. Circled dots mark the 2MASS near-IR positions of IRS 5 and IRS 8 for clarity. Log intensity scale. Coordinates are J2000.

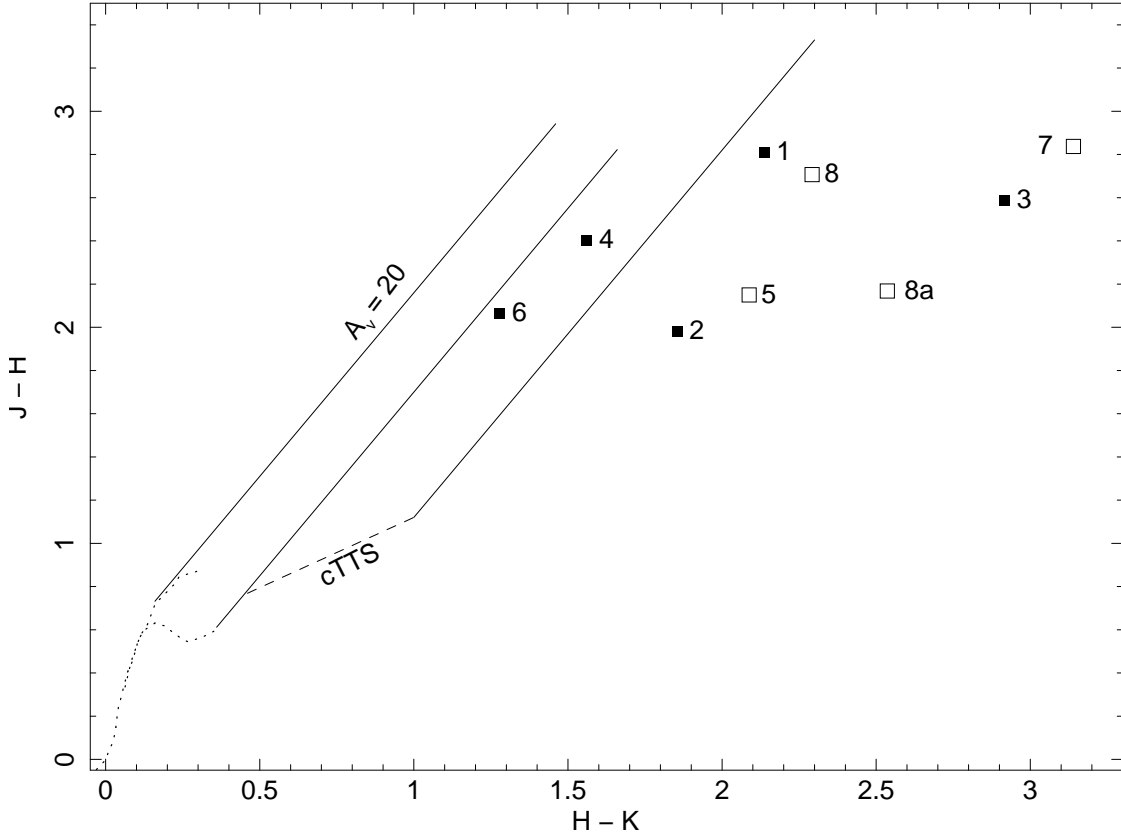


Fig. 3.— Near-IR color-color diagram of NGC 2071-IR sources (Fig. 1). The colors are based on the photometry of Tamura et al. (2007) transformed into the CIT photometric system from the 2MASS system using the transformation of Carpenter (2001). Solid squares are sources detected by *Chandra* (Table 1) and open squares are non-detections. The dotted lines at the lower left are the unreddened colors of dwarf and giant stars based on the intrinsic colors of Bessell & Brett (1988) converted into the CIT system. The dashed line is the classical T Tauri star locus from Meyer et al. (1997) representing the range of intrinsic IR excess for young stars with evidence for accreting circumstellar disks in Taurus. The three solid lines show representative reddening vectors based on Cohen et al. (1981) for $A_V = 20$ mag as measured in the CIT system. The colors of IRS 4 and IRS 6 are consistent with reddened classical T Tauri stars while the rest of the sources appear to have more complex circumstellar environments.

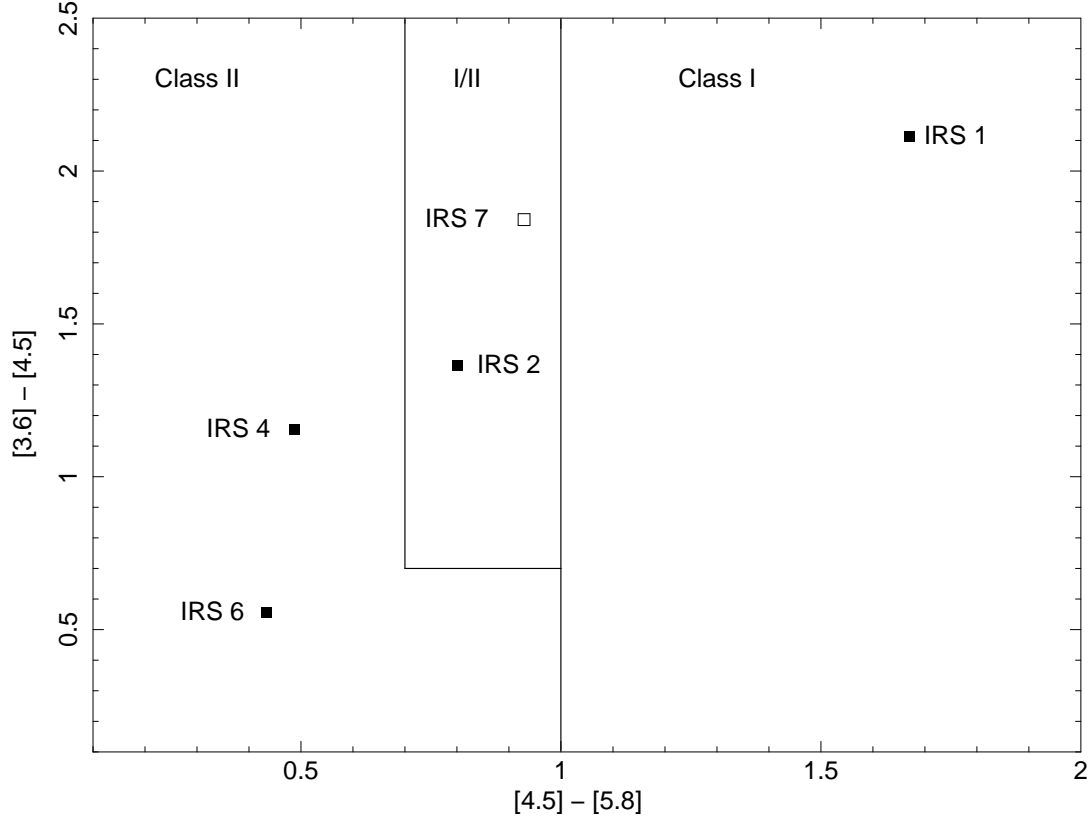


Fig. 4.— IRAC color-color diagram for sources in NGC 2071-IR with measured photometry in all four IRAC bands (Table 2). Solid squares denote sources detected by *Chandra* and the open square marks the undetected object IRS 7. The solid lines show the boundaries between class I, class I or possibly heavily-reddened class II, and class II YSOs based on the criteria of Gutermuth et al. (2008).

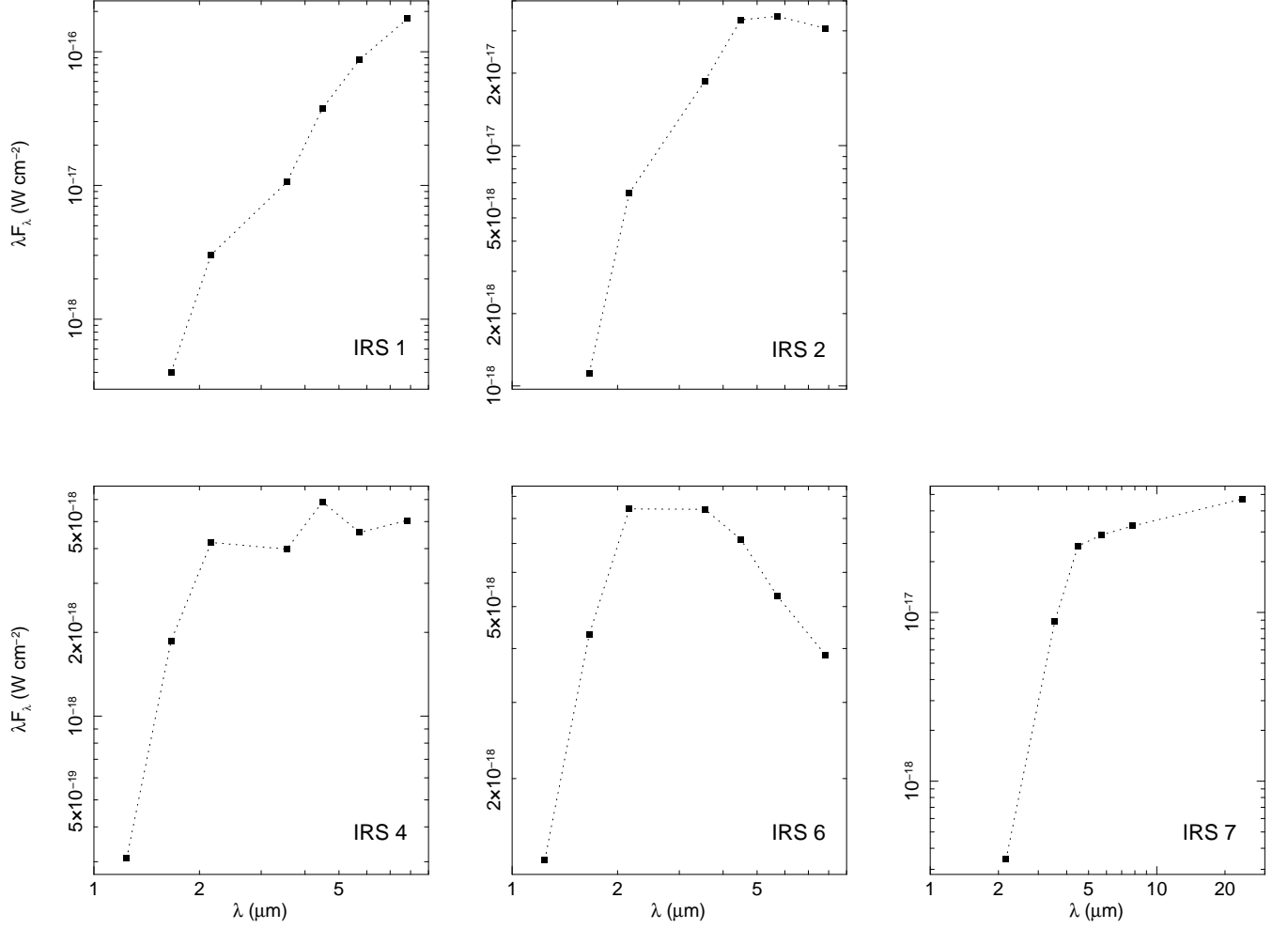


Fig. 5.— Infrared spectral energy distributions of sources in NGC 2071-IR with reliable near-IR and *Spitzer* data. The near-IR data are from *2MASS*. *Spitzer* IRAC data are plotted at 3.55, 4.49, 5.72, and 7.83 μ m. A MIPS-24 measurement is shown for IRS 7 at 23.84 μ m.

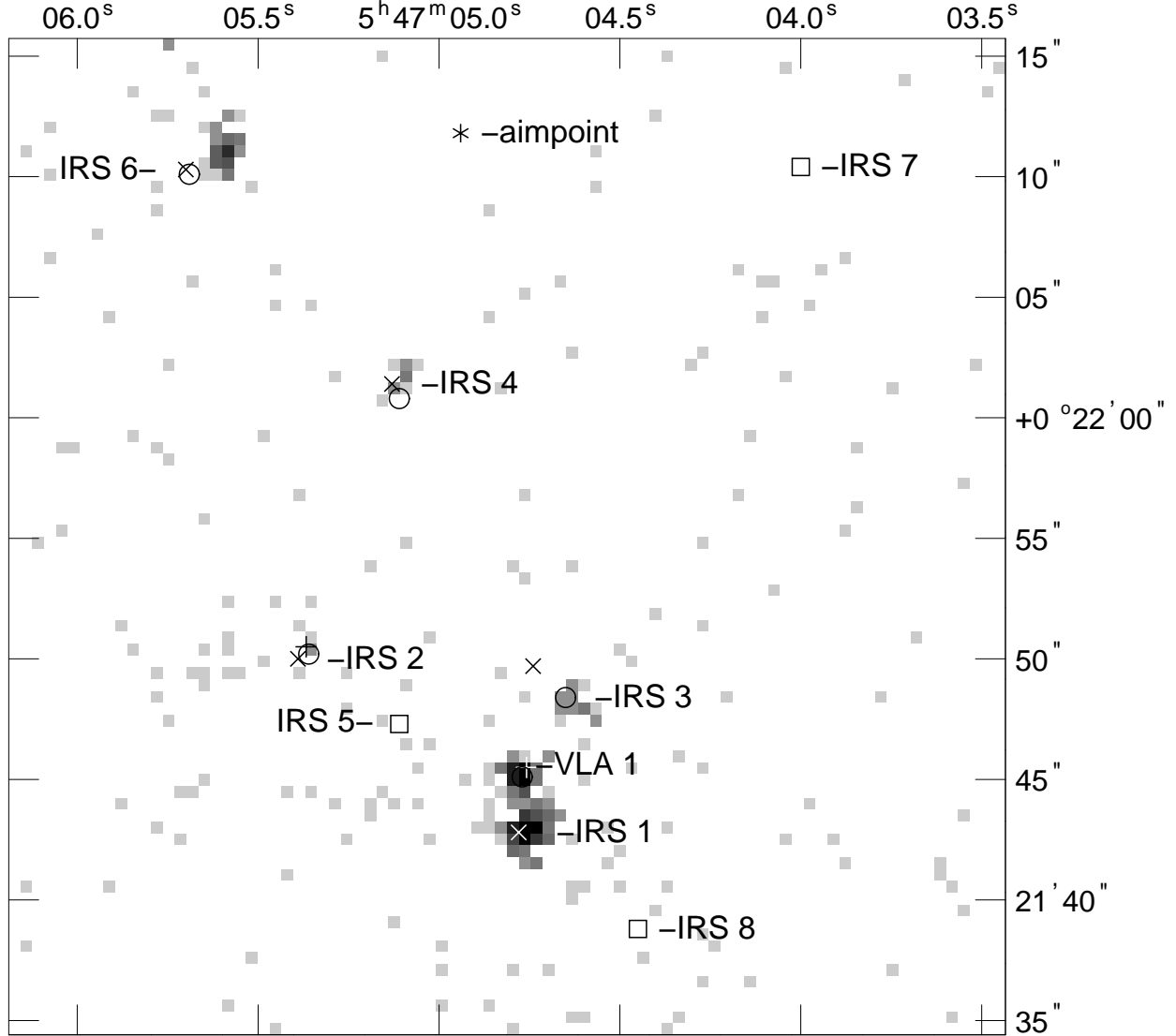


Fig. 6.— *Chandra* ACIS-I image of the central region of the infrared cluster NGC 2071-IR (0.3 - 7 keV, log intensity scale, $0.''49$ pixels, J2000. coordinates). An asterisk marks the *Chandra* aimpoint. The crosses (\times) mark 2MASS source positions of near-IR sources with *Chandra* counterparts (IRS 1,2,3,4, and 6). and open squares mark 2MASS positions of the undetected cluster core sources IRS 5,7, and 8. Circles show the near-IR positions of sources IRS 2, 3, 4, and 6 obtained by applying the offsets given in Walther et al. (1993) to the 2MASS position of IRS 1. Plus signs (+) mark the *VLA* radio positions of VLA 1 and IRS 2A (C. Carrasco-Gonzalez 2009, priv. communication).

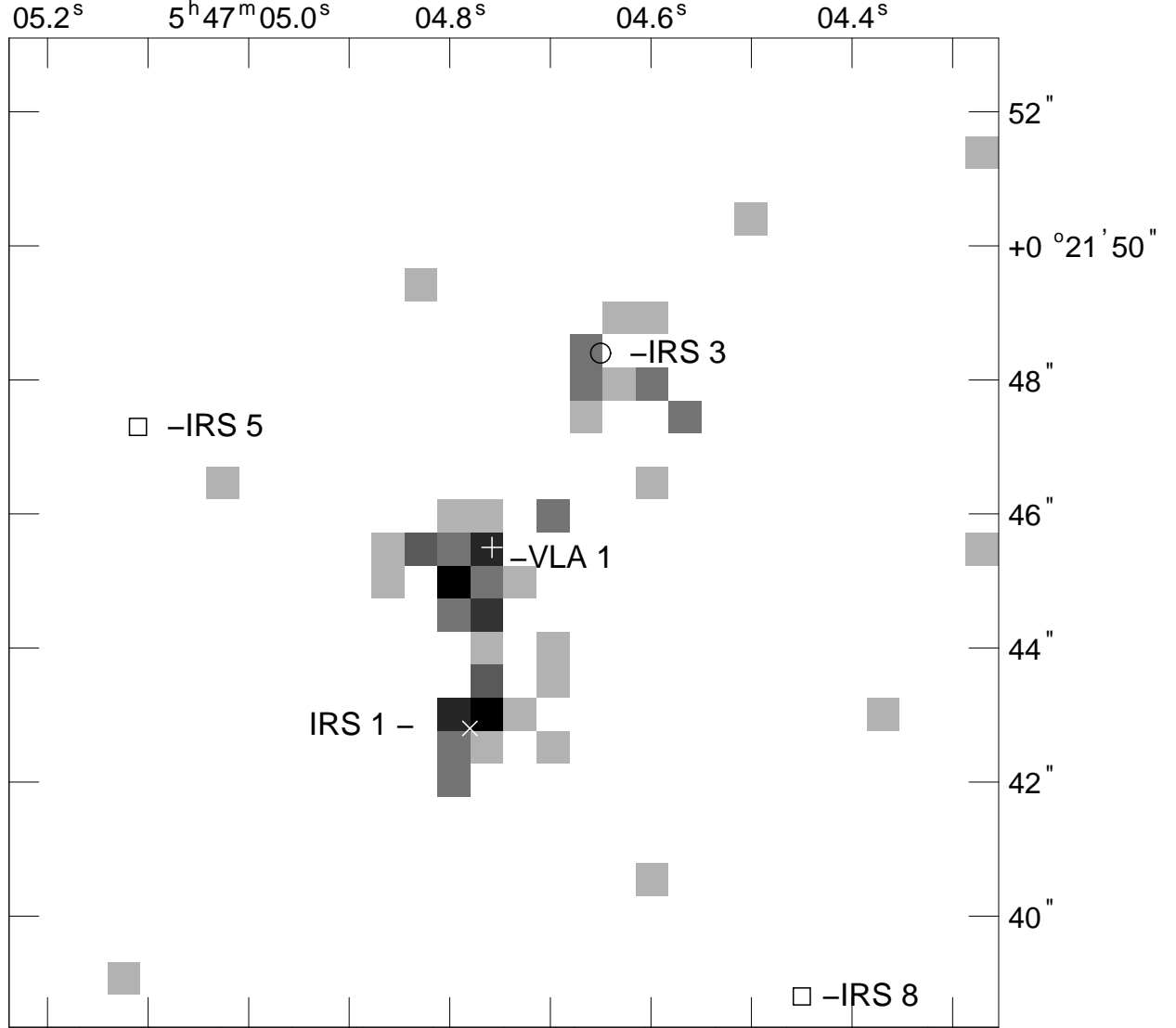


Fig. 7.— Zoomed view of the *Chandra* ACIS-I image near IRS 1 in the hard energy range (4 - 7 keV, log intensity scale, 0.''49 pixels, J2000. coordinates). Symbols are the same as in Fig. 6. Hard emission is detected from IRS 1, IRS 3, and VLA 1. The near-IR sources IRS 5 and IRS 8 were undetected by *Chandra*.

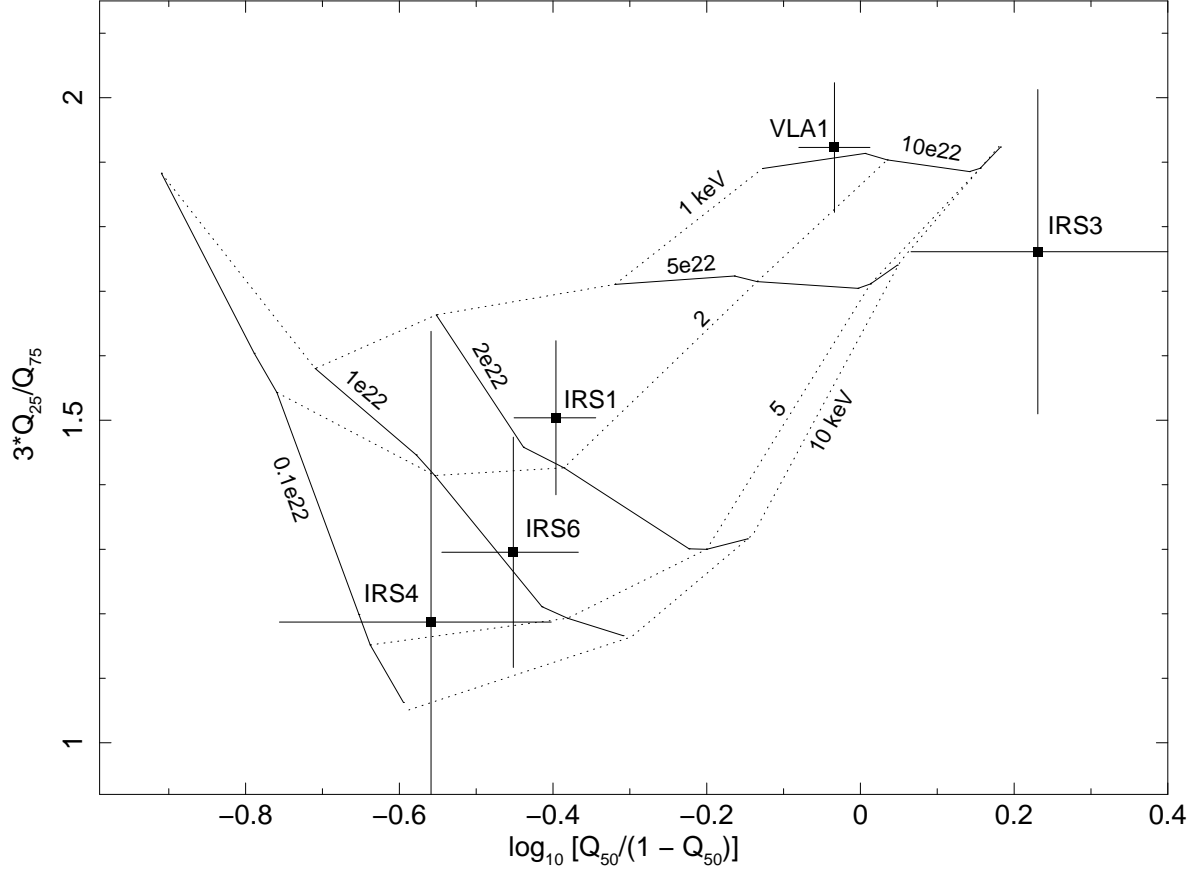


Fig. 8.— Quantile plot of the X-ray sources in NGC 2071-IR. The source IRS 2 (4 net counts) is too faint for quantile analysis and is not shown. The quantile values are defined using the relation $Q_x = (E_{x\%} - E_{lo}) / (E_{up} - E_{lo})$ (Hong et al. 2004), where $E_{lo} = 0.3$ keV and $E_{up} = 7.0$ keV in this study. Solid lines show loci of constant absorption column density $N_H = (0.1, 1, 2, 5, 10) \times 10^{22} \text{ cm}^{-2}$ and dotted lines show loci of constant plasma energy $kT = 1, 2, 5$, and 10 keV. The grid of N_H and kT values was generated using simulations based on a solar-abundance 1T APEC thermal plasma model and the response and auxiliary response files for IRS 1.

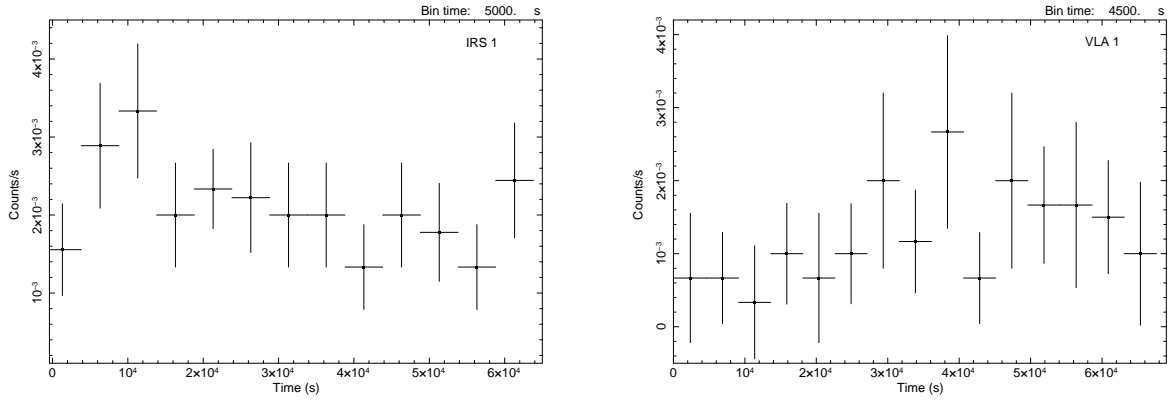


Fig. 9.— *Left:* *Chandra* broad-band (0.3 - 7 keV) ACIS-I lightcurve of IRS 1 binned at 5000 s intervals. The mean count rate is 2.02 ± 0.69 ($\pm 1\sigma$) c ksec $^{-1}$. The KS test gives a probability of constant count rate $P_{\text{const}} = 0.11$, so variability is not demonstrated with high confidence. *Right:* *Chandra* broad-band (0.3 - 7 keV) ACIS-I lightcurve of VLA 1 binned at 4500 s intervals. The mean count rate is 1.33 ± 0.75 ($\pm 1\sigma$) c ksec $^{-1}$. The KS test gives $P_{\text{const}} = 0.02$, so variability is likely.

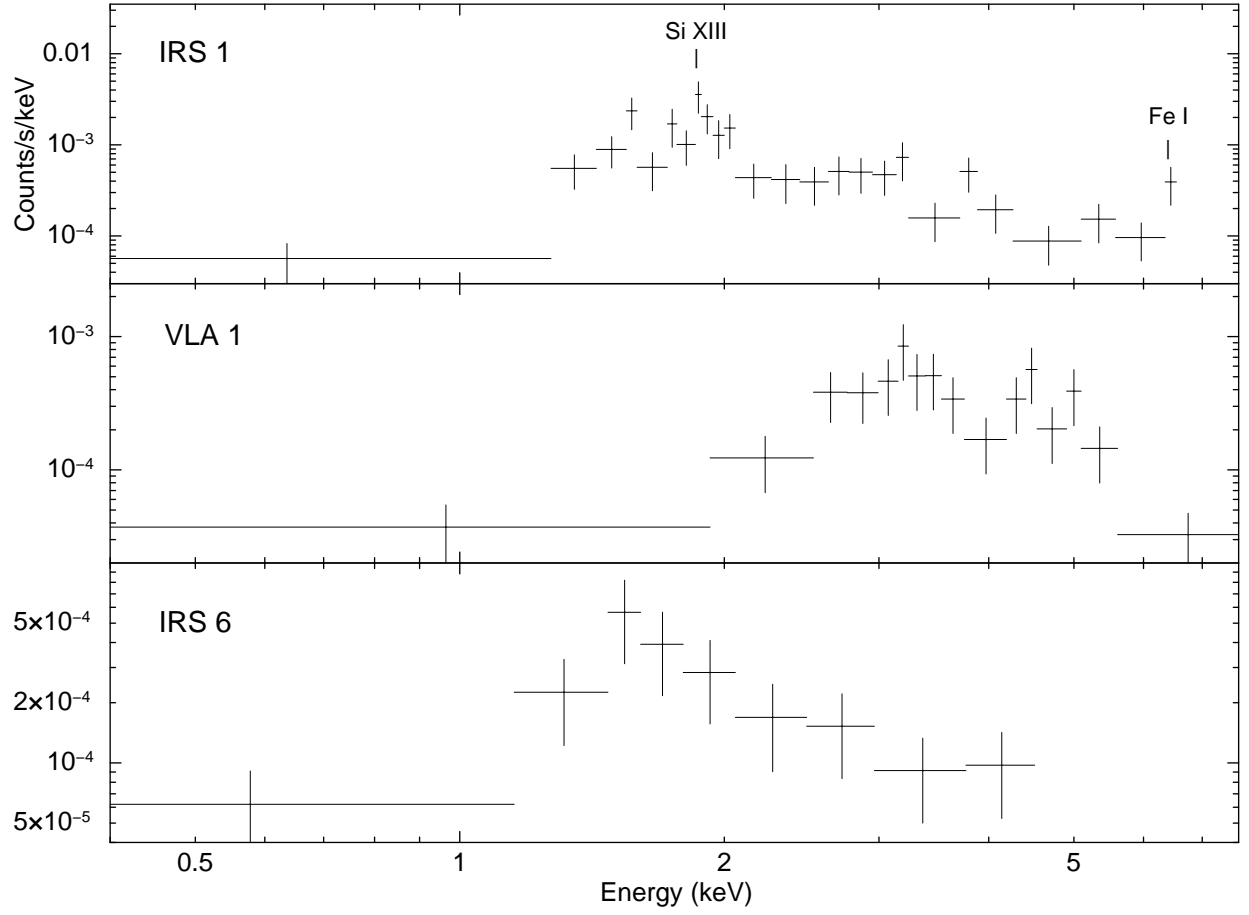


Fig. 10.— ACIS-I spectra of IRS 1, VLA 1, and IRS 6 binned to a minimum of 5 counts per bin.

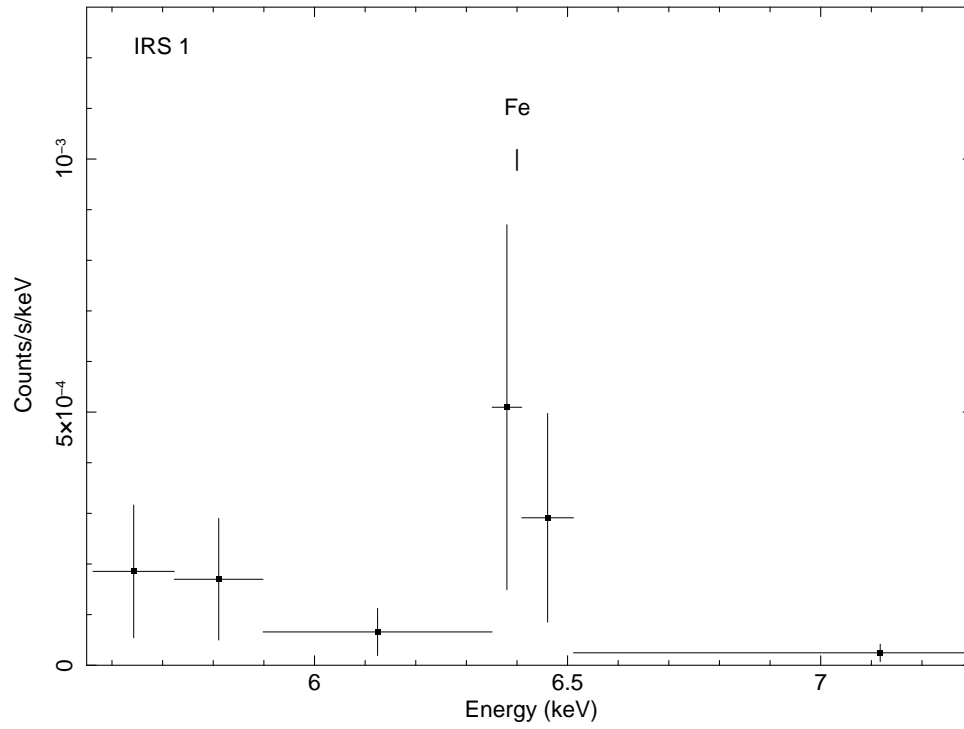


Fig. 11.— ACIS-I spectrum of IRS 1 binned to a minimum of 2 counts per bin, showing the region near the fluorescent iron line. Solid squares are data points.

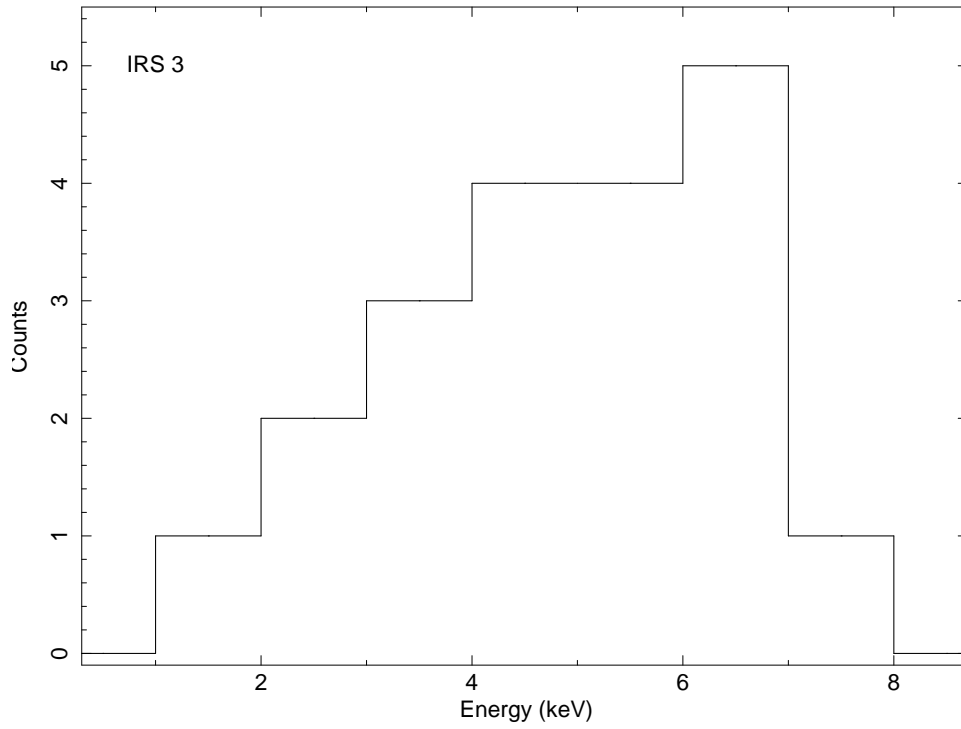


Fig. 12.— ACIS-I event energy histogram of the hard X-ray source IRS 3 using events in the 0.3 - 7 keV range, binned at 1 keV intervals. The extraction region contained 20 events, of which 2 events are likely background. The median event energy is $E_{50} = 4.52$ keV.